# The inflammasome adaptor protein ASC triggers immunometabolic dysregulation induced by dysbiosis during obesity

Martinez-Garcia, JJ[1,2*]; Rodríguez, S[1]; Guijarro, A[1]; Quevedo-Romero, I[1], Mateo, SV[1]; Molina-López, C[1]; Hurtado-Navarro, L[1]; Baroja-Mazo, A[1]; Pelegrín, P[1,2*].

[1]Molecular Inflammation Group, Biomedical Research Institute of Murcia (IMIB), Murcia, Spain

[2]Department of Biochemistry and Molecular Biology B and Immunology, Faculty of Medicine, University of Murcia, Murcia, Spain

***Correspondence to**: jjmartinezgarciaio@gmail.com and pablopel@um.es

**Running title**: ASC controls immunometabolism in obesity

**Abstract**

The innate immune system oversees the response to danger signals. One of the most complexes organs that develops this response is the gut, which is extremely sensitive to the microbial changes in response to high saturated fat diets (HFD), leaving the space to be colonised by opportunistic bacteria, and triggering the innate immune response. Different evidence suggests the potential of the inflammasome in diet-induced inflammation, but little is known about its impact on the gut immunometabolic dysregulation. In this work, we report that the inflammasome adaptor apoptosis speck-like protein with a caspase activation domain (ASC) is essential for the development of obesity and insulin resistance during a high-fat diet (HFD). In ASC-deficient mice (*Pycard*$^{-/-}$), lower weight gain and improved glucose tolerance were observed in comparison to wild type mice. Therefore, the absence of ASC reduces intestinal permeability and improves the benefitial effects of the gut microbiota, decreasing dysbiosis, making the intestinal environment healthier. Additionally, *Pycard*$^{-/-}$ mice presented an enhanced glycolysis and aerobic metabolism, contributing to reduced inflammation, fat accumulation in the liver and improved hepatic metabolic function. Developing therapies targeting ASC could be beneficial to treat obesity, type II diabetes, and metabolism-associated liver diseases.

**Keywords:** ASC, inflammasome, microbiota, metabolism, glucose tolerance, macrophages, intestinal permeability, high-fat-diet

**Abbreviations list:** ASC: Apoptosis-associated Speck-like protein containing a CARD; cDNA: Complementary Deoxyribonucleic Acid; DEG: Differential Expressed Gene; DNA: Deoxyribonucleic Acid; FDR: False Discovery Rate; GO: Gene Ontology; GSDMD: Gasdermin D; GTT: Glucose Tolerance Test; HFD: High-Fat-Diet; IL: Interleukin; LPS: Lipopolysaccharide; mRNA: Messenger Ribonucleic Acid; NCD: Normal-Chow-Diet; NIN1: Ninjurin-1; NLR: Nucleotide-binding domain Leucine-rich Repeat receptor; NLRP: Nucleotide-binding domain Leucine-rich Repeat Pyrin domain-containing receptor; NOD: Nucleotide-binding and Oligomerization Domain; PCA: Principal Components Analysis; PCR: Polymerase Chain Reaction; PBS: Phosphate Saline Buffer; RNA: Ribonucleic Acid; TCA: Tricarboxylic Acids cycle; TLR: Toll-Like Receptor.

## Introduction

Nucleotide-binding domain leucine-rich repeat receptors (NLRs) constitute an important part of the inflammatory response, responding to a wide variety of danger and pathogens associated molecular patterns, especially those ones presented by bacteria(1,2). NLRs, including the most studied NLRP3, are highly expressed in myeloid cells from the immune system as well as in epithelial cells(3). NLRP3 and other NLRs can oligomerize forming inflammasomes that activate caspase-1 to mature the proinflammatory cytokines interleukin (IL)-1β and IL-18(4,5). Caspase-1 also processes the protein gasdermin D (GSDMD), which N-terminal fragment form pores in the plasma membrane initiating the release of IL-1β and IL-18 and an immunogenic programmed cell death termed as pyroptosis(6). During pyroptotic cell death the plasma membrane protein ninjurin-1 (NINJ1) induces membrane rupture(7). Some inflammasomes require interaction and oligomerization of the apoptosis-associated speck-like protein containing a caspase-1 activating domain (ASC) to activate caspase-1. Large inflammasome oligomers of ASC are externalized to the extracellular space during pyroptosis to amplify the inflammatory response(8–13).

The intestinal microbiota plays a crucial role contributing to the host's health and survival(14). This makes the gut extremely sensitive to microbiota changes, which controls colonisation by opportunistic bacteria and triggering innate immune responses, including inflammation(15,16) Subsequently, the effect of the gut microbiome controlling the activity of the inflammasome has been reported with both antibiotics and germ-free (GF) conditions(17,18). The participation of the different inflammasomes, including the NLRP3, has been tightly associated with diet-related metabolic diseases, such as obesity and type II diabetes (19). In this direction, the consume of diets with high saturated fats (HFD) induces an inflammatory reaction and potentiates IL-1β production (20). Furthermore, the NLRP6 inflammasome, which is present in the intestinal epithelial cells, is capable of maintaining the gut microbiota homeostasis through the production of IL-18 (21). Other studies demonstrate the participation of pyroptosis induced by GSDMD as a protective agent that controls the intestinal microbiota and repairs the intestinal mucosa (22). However, there is controversy with the role of pyroptosis in obesity, as it is not only associated with an increase in obesity but is also capable of inducing metabolic dysregulations, such as blockage of cholesterol transport for subsequent catabolic processes, the accumulation of atheroma plaques, and the development of inflammatory diseases such as steatohepatitis (23–25). This disparity highlights that the molecular

77 mechanism by which inflammation is induced by the inflammasome and pyroptosis can affect
78 glucose homeostasis and the development of metabolic pathologies. However, is still not well
79 defined the role of the common inflammasome adaptor protein ASC in these diseases, as
80 oligomers of ASC could be contributing to metabolic dysregulation, being a potential target
81 of study on the field of the immunometabolic cues regulating gut physiopathology.
82 In this study we identify that the deletion of the common inflammasome assembly adaptor
83 protein ASC protects mice in response to a HFD. This effect increases tolerance to glucose
84 and exacerbated glycolytic and aerobic metabolism in HFD conditions, with a decrease of the
85 inflammatory response. It also involves a change of the gut epithelial integrity and
86 permeability, and regulates gut microbiome. This work suggests ASC as a potential therapy
87 to treat obesity, metabolic dysfunction-associated steatotic liver disease, and type II diabetes,
88 which could positively impact on the lifestyle of those patients.

## Results

### *ASC deficiency prevents gain of weight and glucose intolerance under high-fat-diet conditions*

To monitor potential weight changes during the time dependent on the inflammasome, weight from C57/BL6 background wild type (*Pycard*$^{+/+}$) mice togetherand *Pycard*$^{-/-}$ mice from same age was monitored during 5 months in normal chow diet. We observed that the *Pycard*$^{-/-}$ tended to gain less weight than the *Pycard*$^{+/+}$, but it was not significant **(Figure 1A)**. This body weight gain control was found in both males and females, revealing that *Pycard*$^{-/-}$ mice can prevent body weight gain independently on the sex differences **(Suppl. Figure 1A)**. Therefore, we next asked whether ASC deficiency can modulate weight gain in obesity after feeding with a HFD. Weigh of *Pycard*$^{-/-}$ tended to decrease when compared to wild type from the third month of HFD, but it was not significant **(Figure 1B)**. HFD-dependent weight gain was confirmed comparing HFD to normal chow diet (NCD) fed wild type mice **(Suppl. Figure 1B).** To explore if ASC oligomers were functioning extracellularly during HFD feeding, we rescue the ASC-dependent phenotype in *Pycard*$^{-/-}$ with intraperitoneal administration of recombinant ASC oligomers, but this treatment did not increase weight gain to the levels of the wild type **(Figure 1B)**. We next asked whether ASC is involved in the pathologic phenotype observed in metabolic syndrome. We then measured glucose levels in mice feed with HFD and observed an increase of glucose tolerance in the ASC-deficient mice respect to the wild type either at 3 and 5 months after HFD **(Figure 1C,D)**. Glucose tolerance of *Pycard*$^{-/-}$ mice under HFD was independent on the administration of recombinant ASC oligomers **(Figure 1C,D)**. However, ASC oligomers induced a tendency to increase the maximum peak of glycemia at 20 minutes after glucose injection **(Figure 1C,D)**.

### *ASC controls intestinal permeability and peritoneal cell infiltration in high-fat-diet*

As expected, HFD induced intestinal permeability respect NCD fed mice **(Figure 2A)**. However, *Pycard*$^{-/-}$mice fed with HFD presented a significant decrease of intestinal permeability, which was rescued by administration of recombinant ASC oligomers **(Figure 2B)**. In parallel to intestinal permeability increase, we also observed an increase of the number of infiltrated cells in the peritoneum upon HFD respect NCD fed wild type mice **(Figure 2C)**. Surprisingly the *Pycard*$^{-/-}$ mice presented a higher increase of peritoneal cells after 5 months of HFD when compared to wild type, which tended to decrease with the addition of the intraperitoneal recombinant ASC oligomers, but it was not significant **(Figure 2D)**. There was a positive correlation between

120 intestinal permeability and the number of peritoneal cells in *Pycard*$^{+/+}$ mice **(Figure 2E)**, but
121 intestinal permeability did not correlated to the increase of peritoneal cells in *Pycard*$^{-/-}$ mice
122 **(Figure 2F)**, suggesting independent processes.
123 To investigate inflammasome function in infiltrated peritoneal cells during HFD conditions, we
124 cultured adherent peritoneal cells from mice and measure IL-1β in cell supernatants. Peritoneal
125 cells from wild type mice fed with HFD presented IL-1β release by LPS treatment and after
126 classical NLRP3 inflammasome activation **(Figure 2G)**. As expected, IL-1β release induced by
127 nigericin in both NCD and HFD conditions presented a dependency on the NLRP3 inhibitor
128 MCC950 **(Figure 2G)**. However, LPS induced IL-1β release in HFD was also dependent on
129 NLRP3 activity **(Figure 2G)**, suggesting increase sensitivity to activate NLRP3 in peritoneal
130 infiltrated cells after HFD. As expected, IL-1β release in peritoneal cells from *Pycard*$^{-/-}$ mice fed
131 with HFD was decreased when treated with LPS and nigericin, independently of the intraperitoneal
132 injection of recombinant ASC oligomers **(Figure 2H, Suppl. Figure 2A)**. This effect could be due
133 to the metabolization of ASC oligomers in vivo or little capture of these oligomers by peritoneal
134 cells during the 5 months of HFD. As control, IL-6 release from peritoneal cells was independent
135 on the genotype **(Suppl. Figure 2B,C)**. These data suggest that ASC deficiency could protect
136 intestinal permeability during obesity.
137
138 ***ASC deficiency increases gut microbiota biodiversity during high-fat-diet***
139 We next wondered if ASC could control gut dysbiosis induced by 5 months of HFD. We
140 determined 16S RNA in faeces and found that the microbiota composition changed in *Pycard*$^{-/-}$
141 mice fed with HFD in comparison with the *Pycard*$^{+/+}$ mice **(Figure 3A)**. Intraperitoneal
142 administration of recombinant ASC oligomers reverted gut microbiota composition of *Pycard*$^{-/-}$ to
143 the dysbiosis microbial composition induced by the HFD **(Figure 3A)**. This suggests that during
144 HFD, inflammasome oligomers might be eliminated by the intestine where it could impact in gut
145 microbiota composition. Within the most abundant bacteria that was influenced by the deficiency
146 of ASC, we encounter mainly *Akkermansia muciniphila, Blautia coccoides, Romboutsia ilealis*
147 and *Bacteroides acidifaciens*, which constitute approximately 90% of the microbiota biodiversity
148 **(Figure 3A).** In particular, ASC deficiency increase the proportion of *B. coccoides* and decrease
149 *A. muciniphila* when compared to wild type mice, while administration of recombinant ASC
150 oligomers restored this ratio, and also increased *R. ilealis* and *B. acidifaciens* **(Figure 3A)**. We

151 also found that the abundance of Verrucomicrobiota is about the 25% of the microbiota
152 composition in wild type mice under HFD **(Figure 3B)**. However, the ratio of Verrucomicrobiota
153 respect to the other main phylum, Firmicutes and Bacteroidota, decreased in *Pycard*$^{-/-}$ with HFD
154 **(Figure 3C)**. Intraperitoneal administration of recombinant ASC oligomers also rescued phylum
155 ratio, increasing Verrucomicrobiota phyla **(Figure 3D)**. As a quality control, we observed in a
156 different batch of mice that the NCD ASC$^{+/+}$ group presented a very few proportions of
157 Verrucomicrobiota **(Suppl. Figure 3A)**, which strongly increased in HFD conditions **(Suppl.**
158 **Figure 3B)**. Regarding the importance of the low abundance of Verrucomicrobiota to control
159 dysbiosis, and maintain the microbiota biodiversity, *A. muciniphila*, the main bacteria from the
160 Verrucomicrobiota phyla, tended to decrease in *Pycard*$^{-/-}$ mice fed with HFD **(Figure 3E)**.
161 However, other top 5 abundant bacteria, *Bacteroides* did not change the relative abundance
162 **(Figure 3F)**. The decrease of these bacteria left the niche to the colonization of new bacteria that
163 incremented the microbiota abundance, such as *Enteractinococcus* and *Apostotipes* **(Figure 3G**
164 **and 3H)**. For these bacteria, the intraperitoneal administration of recombinant ASC oligomers in
165 *Pycard*$^{-/-}$ mice under HFD rescued dysbiosis, and in the case of *Bacteroides*, it strongly increased
166 the abundance contributing to decrease the microbiota biodiversity **(Figure 3E-H)**. As a control
167 quality, we verified that the abundance of *A. muciniphila* in wild type HFD conditions tended to
168 increase respect the NCD fed controls **(Suppl. Figure 3C)**. These data corroborated that *Pycard*$^{-/-}$
169 mice prevent the dysbiosis, creating a benefitial environment in the gut by the lack of extracellular
170 ASC oligomers.
171
172 ***ASC induces bacteria attachment in intestinal villi during high-fat-diet***
173 Since the absence of ASC reduces intestinal permeability and prevents the dysbiosis, we next
174 studied if the intestinal mucosa was involved in the regulation of this phenomenon under HFD.
175 We observed that wild type mice fed with HFD presented a severe bacterial colonization in the
176 small intestinal *villi* **(Figure 4A)**. Bacteria attached to the *villi* decreased in ASC-deficient mice,
177 and mucus was present in the border of each intestinal *villi* **(Figure 4B)**. When recombinant ASC
178 oligomers were intraperitoneally injected on *Pycard*$^{-/-}$ mice with HFD, the number of bacteria
179 within the intestinal *villi* was not rescued **(Figure 4C)**, but mucus was absent in comparison with
180 the *Pycard*$^{-/-}$ mice without recombinant ASC oligomers administration **(Figure 4C)**. This suggests
181 that extracellular ASC oligomers partially rescue the protective effect induced by the absence of

182 endogenous ASC. As a control, when the intestinal *villi* of wild type mice fed with HFD were
183 compared with the NCD fed mice, we observed a normal intestinal histology with low bacteria in
184 *villi* and abundant mucus under NCD **(Suppl. Figure 4A,B)**.
185 Bulk RNA sequencing in the small intestine of mice fed with HFD demonstrated that the *Pycard*$^{-}$
186 $^{/-}$ mice have increased expression of metabolic, insulin degrading enzyme and protein synthesis
187 transcript genes (*Gdpd3* and *Ide*) **(Figure 4D)**. ASC deficiency also resulted in a decreased
188 expression of genes related with intestinal inflammation and cancer (e.g. *Ern2)*, epithelial integrity
189 (e.g. *Slc26a6 or Nts)*, hypoxia (e.g. *Ddit4)*, and chemokines produced in response against bacteria
190 (e.g. *Ccl7)* **(Figure 4D)**. Principal component analysis (PCA) was conducted to visualize sample-
191 level clustering based on the expression of the top 20 genes **(Suppl. Figure 4E)**. Administration
192 of recombinant ASC specks in *Pycard*$^{-/-}$ mice during HFD partially rescued gene expression profile
193 in the gut towards wild type genotype **(Figure 4D)**. Gene Ontology (GO) analysis from the
194 differential expressed genes in the small intestine revealed that meanwhile the most enriched
195 pathways in the HFD fed *Pycard*$^{-/-}$ mice were the regulation of the T cell response and the
196 regulation of the MHC class I and II activity, on *Pycard*$^{+/+}$ mice, the AIM2 and NLRP3
197 inflammasome, hormonal activity and positive regulation of the humoral immune response were
198 between the top 10 highly expressed pathways **(Figure 4E)**. Supporting this, the concentration of
199 IL-1β in small intestine decreased in *Pycard*$^{-/-}$ feed with a HFD compared with wild type **(Figure**
200 **4F)**. Intraperitoneal administration of recombinant ASC oligomers reverted IL-1β production in
201 the intestine **(Figure 4F)**. However, IL-6 production did not experimented significant changes in
202 *Pycard*$^{-/-}$ mice **(Suppl. Figure 4C)**. We confirmed that there is not ASC gene expression during
203 the administration of recombinant ASC oligomers **(Suppl. Figure 4D)**. All together summarizes
204 that small intestine mucosa in absence of extracellular ASC oligomers initiates a protective
205 mechanism under HFD reducing innate immunity, increasing epithelial integrity and the aerobic
206 environment, together with the decrease of bacteria and the reduced intestinal permeability.
207

208 ***ASC deficiency increases the glycolytic and tricarboxylic acids pathway in the small intestine***
209 ***under high-fat-diet***

210 As the RNA sequencing revealed a tendency to increase some metabolic genes under HFD
211 treatment, which could also explain the elevation of IL-1β expression, we then analyzed in the
212 small intestine the expression of key metabolic genes related with the glycolysis and the

213 tricarboxylic acids (TCA) cycle. Interestingly, we found that the glycolytic *Pkm2* gene coding for
214 the pyruvate kinase enzyme was highly expressed in the *Pycard*$^{-/-}$ HFD fed mice **(Figure 5A)**.
215 Contrarily, the anaerobic respiration-related gene *Ldha*, corresponding to lactate dehydrogenase,
216 was decreased in the *Pycard*$^{-/-}$ mice **(Figure 5B).** Consequently, we observed an increase
217 expression of *Pdha* gene, which encodes the pyruvate dehydrogenase enzyme **(Figure 5C)**. This
218 observation could indicate that the high glycolytic state on the *Pycard*$^{-/-}$ mice small intestine under
219 HFD drives to the aerobic metabolism, and not to the anaerobic pathway. To verify this switch,
220 we also analyzed the intestinal gene expression of the enzyme that belonged to the TCA cycle. We
221 reported that *Glud1* and *Sdha* genes expression generally was increased in the *Pycard*$^{-/-}$ HFD mice
222 **(Figure 5D,E)**. We also demonstrated that the β-oxidation-related gene *Cpt1a* expression
223 increased in *Pycard*$^{-/-}$ HFD mice respect the wild type **(Figure 5F)**. These results aligns with the
224 fact that the *Pycard*$^{-/-}$ have decreased weight and increased glucose tolerance independently on the
225 HFD due to a high catabolism and energy uptake. This effect was dependent on the extracellular
226 function of oligomers of ASC, as the intraperitoneal administration of recombinant ASC oligomers
227 tended to revert the elevated catabolic environment towards the levels of the wild type mice
228 **(Figure 5A-F)**.
229
230 ***ASC deficiency enhances hepatic metabolism and reduces inflammation, bile acids and fat***
231 ***accumulation under high-fat-diet***
232 We finally investigated if *Pycard*$^{-/-}$ mice have an altered liver physiopathology and metabolism
233 during HFD. Initially we observed that wild type mice fed with HFD presented an exacerbated fat
234 accumulation in the liver **(Figure 6A)**. Liver fat accumulation was absent in ASC-deficient mice
235 under HFD **(Figure 6B)**. Differentially to the effects observed in the small intestine, intraperitoneal
236 administration of recombinant ASC oligomers did not rescue wild type phenotype **(Figure 6C)**,
237 suggesting that extracellular ASC oligomers might impact small intestine, but not hepatic
238 physiopathologic consecuences, that might be controlled by intracellular ASC. The accumulation
239 of hepatic fat under HFD in wild type was corroborated when compared with NCD fed mice
240 **(Suppl. Figure 5A,B)**. Moreover, we observed increased expression of metabolic genes in the
241 liver of *Pycard*$^{-/-}$HFD fed mice, in particular genes related with the PPARα signaling pathway
242 **(Figure 6D)**, the electron transport chain from the mitochondrial respiration **(Figure 6E)**, and the
243 synthesis of aminoacids derived from the TCA **(Figure 6F)**. Interestingly, we observed a decrease

244 expression of the classical bile acid synthesis enzyme *Cyp7a1* gene **(Figure 6G)**, which was
245 confirmed when we measured the opposite effect on the *Shp* gene expression **(Figure 6H)**.
246 Similarly to the small intestinal mucosa, in the liver there was also a tendency to decrease IL-1β
247 production in the *Pycard*$^{-/-}$ mice fed with HFD **(Figure 6I)**. Similar to hepatic fat accumulation,
248 the administration of recombinant ASC oligomers were not able to rescue gene expression in the
249 liver of *Pycard*$^{-/-}$ mice **(Figure 6D-I)**, supporting the idea that extracellular ASC oligomers do not
250 impact liver during HFD.
251 Overall, ASC is important to control metabolic syndrome induced by HFD, with a dual role, being
252 intracellular ASC intestine permeability, obesity, glucose tolerance and hepatic inflammation,
253 metabolism and steatosis; while extracellular ASC oligomers modulate dysbiosis and metabolism
254 and inflammation in the small intestine.

255 **Discussion**

256 In this study we found that ASC deficiency causes a protective effect during HFD on associated
257 obesity and metabolic syndrome effect. This protection was observed at different levels, including
258 the decrease of intestinal permeability, dysbiosis, changes in the integrity, metagenomic,
259 metabolism and physiology of the small intestine epithelia, and a robust decrease of the IL-1β
260 production. This protective effect was also found in the hepatic metabolism, inflammation and
261 steatosis. Dysbiosis, intestinal metabolism and IL-1β production were reverted in the *Pycard*$^{-/-}$
262 mice when recombinant ASC oligomers were intraperitoneally administrated, suggesting a
263 differential role of extracellular ASC oligomers for microbiota, intestine and hepatic functions.
264 Recent developments of nanobodies-targeting extracellular ASC oligomers (11) might be
265 beneficial to treat dysbiosis associated to HFD.

266 We initially observed that the *Pycard*$^{-/-}$ mice fed with a HFD reduced obesity and increased glucose
267 tolerance. But even the weight gain did not increase with the intraperitoneal addition of
268 recombinant ASC oligomers, glucose tolerance tended to increase during the maximum glycemia
269 peak, at 20 minutes after the glucose injection. This effect let us conclude that the protective effect
270 of ASC depletion could be mediated by a mechanism of regulation which partially depends on the
271 inflammasome induced ASC oligomerization and release. Extracellular ASC oligomers have been
272 detected extracellularly in different pathologies, including autoinflammatory syndromes,
273 amyloidosis, Alzheimer disease, and HIV infection (8,9,11,12,26). However, pathological
274 consequences of the metabolic syndrome appearing at long term, including obesity and the
275 steatosis (27,28), are not affected by the presence of extracellular ASC oligomers, being probably
276 dependent on the intracellular functions of ASC.

277 Previous studies have reported a relation between intestinal permeability and immune function of
278 peritoneal cells (29), which can be supported by the fact that during HFD intestinal permeability
279 positively correlated with the number of infiltrated peritoneal cells found in our study. Conversely,
280 we found an increase of peritoneal cells in the absence of ASC, probably as consequence of the
281 reduced cell death of peritoneal cells upon inflammasome activation (30). The decrease in
282 intestinal permeability might be related to the gut microbiota (31). Indeed, our results revealed that
283 a HFD impact intestinal microbiota biodiversity, increasing the abundance of species of the
284 Verrucomicrobiota Phylum, including *A. muciniphila*, a mucin-degrading bacteria which normally
285 is benefitial, but in excess, it can dysregulate gut homeostasis (32–34). It is important to consider

286 that the pathological consequences of HFD could not be only attributed to *A. muciniphila*, but
287 maybe to a role of a homeostatic regulator of *A. muciniphila,* when either the excess or the low
288 abundance of this bacteria can be prejudicial. Moreover, the decrease of this bacteria in the gut
289 free a niche that can be colonised by less abundant bacteria, reducing dysbiosis and increasing the
290 microbial biodiversity as we observe for the *Pycard*$^{-/-}$ HFD fed mice group. As an example, the
291 decreasing mucus can reduce the attachment of segmented filamentous bacteria, which induces an
292 immune response to maintain homeostasis of the intestinal mucosa (35). The protection of
293 dysbiosis by the deficiency of ASC was also corroborated at histological level, where ASC
294 deficiency prevented the inclusion of bacteria in the intestinal mucosa, with an increase of mucus
295 between the intestinal *villi*. Additionally, administration of recombinant ASC oligomers rescue the
296 dysbiosis found in the wild type mice induced by HFD and also depleted the mucus formation,
297 which is mediated by the goblet cells from the intestinal mucosa (36). Concomitantly with this
298 effect, ASC controlled intestinal epithelia gene expression related with the innate immune response
299 against pathogens, inflammation, and the epithelial integrity, some of them are considered as
300 markers for obesity and cancer (37–39). Moreover, the increasing expression of the insulin
301 degrading enzyme (*Ide*) gene that we observed in *Pycard*$^{-/-}$ mice under HFD could explain the
302 increasing tolerance to glucose, as this enzyme protects from insulin resistance, and obesity in
303 response to high glycemia levels (40,41). Additionally, the intestinal production of IL-1β was
304 reduced in ASC deficient mice could be attributed to the NLRP3 inflammasome activation, as
305 previous studies have found (17,42). We do not discard that other inflammasomes, which are
306 highly expressed in intestinal epithelia can contribute either directly or indirectly to IL-1β
307 production (43–45).
308 Our study also found that small intestinal cells presented an exacerbated catabolic pathway in
309 *Pycard*$^{-/-}$ mice. This might be due because the increase glucose tolerance in an environment with
310 high energy can be a consequence of the augmented glycolytic pathway and TCA through the
311 enzyme's pyruvate kinase and pyruvate dehydrogenase, and decreasing anaerobic lactate
312 dehydrogenase activity. It is important to highlight that even if there is a controversy with the
313 PKM2 isoform, as it is described as an inflammatory potentiator and as inducer of lactate
314 dehydrogenase activity (characteristic of the Warburg effect), this is the PK isoform which is
315 predominant in the intestinal epithelia, and its presence could bypass between the high glycolysis
316 state and the elevated production of IL-1β that we observed in the *Pycard*$^{+/+}$ HFD fed mice, or the

317 increasing TCA, depending on the dimeric or tetrameric forms of PK respectively (46,47). This
318 regulation of glycolysis could reduce fat accumulation in the liver, and might increase hepatic
319 metabolism (48). In the liver of *Pycard*$^{-/-}$ HFD fed mice we also observed a reduction of IL-1β
320 production. The increased metabolism found in the liver could be the consequence to reduce fat
321 accumulation, in a very similar manner as occurs for the small intestine.
322
323 In summary, we report a mechanism of protection to the hyperglycaemic, westernized and high-
324 saturated fat diets which is dependent on the deficiency of the inflammasome adaptor protein ASC.
325 This mechanism is characterized by an exacerbated glucose metabolism together an increasing
326 inflammatory phenotype and a decreasing intestinal permeability by the prevention of dysbiosis
327 and mucus degradation. This mechanism has positive physiological consequences, reducing
328 obesity and increasing glucose tolerance and reducing type II diabetes, and reducing metabolic
329 dysfunction-associated steatosis liver disease, . The presence of extracellular ASC oligomers
330 partially restored the beneficial effects of ASC deficiency on the metabolic syndrome, particularly
331 at intestinal level and dysbiosis, but not in the liver. Further studies are warranted to evaluate
332 potential therapeutic approximations based in the inhibition of ASC oligomerization.
333
334

335 **Materials and Methods**

336 ***Animal Models.*** Animal studies were approved by the regional statement, the Animal Health
337 Service of the General Directorate of Farming, Fishing and Aquiculture of the Council of Murcia
338 (CARM, ID code Nº A13211201) once were positively valuated by the Animal Experimentation
339 Ethics Committee (CEEA) of the University of Murcia (#738/2021) according to the 53/2013
340 Royal Decree and the 32/2007 National Law. Mice were bred in specific pathogen-free conditions
341 with a 12:12 hr light-dark cycle in the animal facility from the University of Murcia, according to
342 governmental guidelines No. 86/609/CEE. Age and gender-matched ASC-deficient (PYCARD-/-
343 ) and wild type C57BL6/J (*Pycard*$^{+/+}$) backgrounds mice were provided to a free access to a
344 standard laboratory chow diet. For the obesity model, mice were fed with a 60% Fat HFD (D12492,
345 Research Diets). Mice were autopsied after euthanasia with Isoflurane and cervical dislocation
346 according to the ethical protocols of the national and international animal experimentation
347 guidelines. After sacrifice, feces, peritoneal exudates, the right lobule of the liver, 1 cm of the
348 proximal small intestine and blood samples were recovered. All samples were recovered strictly
349 in the morning between Zeitgeber Time (ZT)0 and ZT4, to avoid the interference of the circadian
350 changes. Histological samples were collected on Paraformaldehyde 4% diluted from the 32% stock
351 (Sigma-Aldrich, Burlington, MA) at room temperature. For RTqPCR samples, tissues were
352 collected on RNA later (Qiagen, Germany) and frozen on liquid Nitrogen. Feces were collected in
353 a dry tube and frozen on liquid Nitrogen. Peritoneal cells were collected on Phosphate Saline
354 Buffer (PBS) and kept at 4ºC. Plasma was collected in Heparin tubes (Microvette® CB 300 LH,
355 Sarstedt, Germany). For longer tissue storage, samples were stored at -80ºC.

356

357 ***In vivo treatments and tests***. Counted oligomers were diluted into 1x PBS at a concentration of
358 $4x10^6$ oligomers per 100µl, ready to use it in vivo. ASC Oligomers were weekly injected
359 intraperitoneally at a concentration of $4x10^6$ oligomers per mouse. Glucose Tolerance Test (GTT)
360 was done at 3 and 5 months after the administration of the HFD upon gender and sex matched
361 animals. Prior the GTT assay, animals were fasted the day before during 14 hours to avoid the
362 food interference on the glucose levels. Basal fasted glycemia was measured before the Glucose
363 treatment. Following, 1g/Kg of D-Glucose (Sigma-Aldrich) was intraperitoneally injected in each
364 mouse, and glycemia was measured every 20 minutes, minimum during one hour. The last point
365 was measured at 90 minutes after the glucose injection. At the end of the experiment, mice were

366 fed back again. For the intestinal permeability assay, mice were deprived of drinking water during
367 one hour at ZT0. Immediately, 4KDa-FITC were administered orally by gavage at a concentration
368 of 600mg/Kg of mouse. The following hour, blood was collected in the moment of the sacrifice,
369 and plasma was obtained by centrifugation at 2000rcf during 8 minutes.
370
371 ***ASC oligomers purification***. ASC Oligomers were produced and purified as we previously
372 described in Alarcón-Vila et al. 2024 (doi:10.1038/s44321-024-00176-1) (10).
373
374 ***Cells and Treatments.*** $5x10^5$ peritoneal myeloid cells were seeded overnight into each well from
375 a 24 wells plate at 1 million/mL concentration (lymphocytes also were added but were not included
376 into the count). The following day, supernatant was removed, leaving the attached cells for the
377 treatment. *Escherichia coli* LPS 055:B5 (Sigma-Aldrich) was added at 1μg/mL during 4 hours.
378 After priming, supernatant was removed and Nigericin (Sigma-Aldrich) was added at 10μM in E-
379 total buffer (147 mM NaCl, 10 mM HEPES, 13 mM glucose, 2mM CaCl2, 1mM MgCl2, and
380 2mM KCl, pH 7.4) during 30 minutes. MCC950 (Sigma-Aldrich) was added simultaneously to the
381 treatments at 10μM.
382
383 ***Tissue lysates preparation.*** Liver and Small intestines previously stored at -80ºC were
384 mechanically lysed and kept on ice. After being centrifuged at 13200rpm during 10 minutes.
385 Supernatant was recovered. Protein concentration was measured using the Bradford reagent
386 (Sigma Aldrich).
387
388 ***ELISA determinations.*** After In vitro stimulations, supernatants from the peritoneal cells were
389 collected and centrifuged at 13200rpm for 30 seconds. IL-1β and IL-6 were measured in the
390 supernatants using the mouse Quantikine™ ELISA kits, catalog number MLB00C-1 and M6000B
391 respectively (R and D Systems, Minneapolis, MN) following the manufacturer indications, and
392 results were analysed in a Sinergy MX plate reader (BioTek, Winooski, VT).
393
394 ***Histological samples preparation and analysis.*** Liver and small intestine were fixed in 4% p-
395 formaldehyde for 24 hr, processed, paraffin-embedded, and sections stained with haematoxylin

396 and eosin using standard methods to evaluate damage. Slides were examined using a Zeiss Axio
397 Scope AX10 microscope with an AxioCamICC3 (Carl Zeiss, Germany).

398

399 ***RNA extraction and RTqPCR determination.*** RNA was isolated using the RNA mini-extraction
400 kit according the manufacturer guidelines (Qiagen). Cell lysis was performed with the addition of
401 RLT buffer supplemented with β-mercaptoethanol. RNA integrity and concentration were
402 assessed using the NanoDrop spectrophotometer (Thermo Fisher Scientific, Waltham, MA)
403 Isolated RNA was reverse-transcribed with the iScript™ cDNA Synthesis Kit (BioRad, Hercules,
404 CA) according to the manufacturer's instructions. The resulting complementary DNA (equivalent
405 to 500 ng of total RNA) was amplified using the mix SYBR Green Premix ExTaq (Takara) and
406 detected at real time on the iCyclerMyiQ thermocycler (BioRad). Quantitative PCR was performed
407 using forward and reverse primers (sequences available in the web of Sigma-Aldrich). On
408 completion of the PCR amplification, a DNA melting curve analysis was carried out to confirm
409 the presence of a single amplicon. *Actb* gene was used as a reference gene to normalize the
410 transcript levels. Relative mRNA levels (2- DDCt) were determined by comparing the DCt values
411 for treated and control groups (DDCt). Primers for each gene were purchased from Sigma-Aldrich.

412

413 ***RNA Library preparation and sequencing.*** RNA libraries were prepared using the QuantSeq 3′
414 mRNA-Seq Library Prep Kit (Tecan Genomics, Redwood City, CA), with Unique Dual Indices
415 (12nt), CA, following the manufacturer's protocol. Briefly, 500 ng of total RNA per sample was
416 used as input for poly(A) mRNA capture using oligo-dT beads. Captured mRNA was fragmented
417 and reverse-transcribed into cDNA. Second-strand synthesis and adapter ligation were performed
418 to generate double-stranded cDNA libraries. Libraries were indexed with 12-nucleotide unique
419 dual indices for multiplexing and amplified using polymerase chain reaction (PCR). The quality
420 and quantity of the final libraries were evaluated using the Agilent 2100 Bioanalyzer and the Qubit
421 4 Fluorometer (Thermo Fisher Scientific). Libraries were sequenced on a NextSeq 2000 system
422 (Illumina, San Diego, CA) in paired-end mode with a read length of 2 × 100 bp to a target depth
423 of 30 million reads per sample.

424

425 ***RNAseq analysis.*** For RNAseq-Data processing and alignment, Raw sequencing data were
426 processed using the bcl2fastq software (Illumina) to demultiplex and convert base call files into
427 FASTQ format. Quality control of the FASTQ files was performed using FastQC (v0.11.9) to
428 assess read quality, adapter content, and GC distribution. Low-quality reads and adapter sequences
429 were trimmed using Trimmomatic (v0.39). Cleaned reads were aligned to the mouse reference
430 genome (GRCm39) using STAR (v2.7.10a) with default parameters, generating BAM files for
431 each sample. For the differential gene expression, Gene expression quantification was performed
432 using featureCounts (v2.0.3) to obtain raw read counts per gene, based on the GENCODE M28
433 annotation. Count data were provided in a tab-delimited file containing unique read counts for
434 each gene across samples. The dataset was preprocessed using R (R Core Team, 2023). Gene count
435 matrices were normalized using the DESeq2 package (49), which applies a variance-stabilizing
436 transformation to adjust for sequencing depth and RNA composition biases. Differential gene
437 expression analyses were performed using DESeq2's generalized linear model framework,
438 considering the experimental condition as the primary variable. To identify the top differentially
439 expressed genes, the normalized counts were z-score transformed. Heatmaps of the top 20
440 differentially expressed genes were generated using the pheatmap package (50), with sample group
441 annotations included for clarity. Gene identifiers were converted to gene symbols using the
442 org.Mm.eg.db annotation database (51). The PCA was performed using the prcomp function in
443 R, and the resulting components were plotted using ggplot2 (52). Pathway enrichment analysis
444 was performed on differentially expressed genes (DEGs) using the Cluster Profiler package
445 (v4.8.1) in R. Gene Ontology (GO) biological processes were analyzed, with pathways considered
446 significant at a false discovery rate (FDR) $< 0.05$. The selected resulting pathways were visualized
447 using dot plots generated with ggplot2 (v3.4.0). Pathway enrichment analysis was performed on
448 DEGs using the Cluster Profiler package (v4.8.1) in R. Gene GO biological processes were
449 analyzed. The resulting pathways were visualized using dot plots generated with ggplot2 (v3.4.0).
450

451 ***Bacterial DNA extraction.*** Fecal samples were collected directly from the bedding-free cage floor
452 to avoid contamination. Immediately after collection, fecal samples were frozen at −80 °C until
453 further processing. Bacterial DNA from feces was extracted using the Purelink$^{TM}$ Microbiome
454 DNA Purification Kit (Thermo Fisher Scientific), according to the manufacturer instructions. The

concentration and purity of extracted DNA were assessed with a NanoDrop spectrophotometer (Thermo Fisher Scientific).

***16S ribosome RNA gene amplification, sequencing, and metagenomic analysis.*** For the amplification of the 16S rRNA gene, primers targeting the V3-V4 hypervariable regions were designed to cover the bacterial domain (84.2%), archaea (75.8%), based on the SILVA database (March 2020). PCR reactions were performed using 10 ng of DNA as input, combining targeted amplification with barcode addition for sample multiplexing. The resulting amplicons were approximately 606 base pairs in length. The amplification process utilized the Quick-16S Plus NGS Library Prep Kit (Zymo Research) according to the manufacturer's instructions. Following amplification, libraries were pooled in equimolar volumes and purified using magnetic beads to remove residual primers and small fragments, as specified by the kit's protocol. Sequencing of the libraries was performed on the NextSeq 2000 platform (Illumina, San Diego, CA) using a paired-end (2x300 bp) approach. This setup ensured high-resolution reads suitable for downstream taxonomic and functional analyses. A minimum of 50,000 reads per sample was targeted to achieve sufficient depth for robust microbial community profiling. For the bioinformatic analysis, the raw data was first quality controlled by trimming low-quality bases and removing adapters using Trimmomatic. Next, the sequences were denoised and chimeras were removed using the DADA2 algorithm implemented in QIIME 2. Following denoising, the sequences were assigned taxonomy at the genus level using the SILVA v138 database and a Naïve Bayes classifier, which classifies each ASV based on its sequence similarity to known reference sequences. Phyloseq package was used to create a phyloseq object from the ASV table, taxonomic classification, and metadata. The data was then aggregated at the genus level using the tax_glom() function, and relative abundances were calculated using the transform_sample_counts() function in the phyloseq package. The entire workflow was performed using the phyloseq, ggplot2, dplyr, and writexl R packages (52,53).

***Statistical analysis.*** For two variables analysis, normality tests Shapiro-Wilk and Kolmogorov-Smirnov were used to elucidate parametric and non-parametric groups. Where at least, one of the independent groups was non-parametric, non-parametric analysis was used. For testing differences between two independent groups, Mann-Whitney test was used for non-parametric data, and

Student T test was used for parametric data. For testing differences between 3 or more independent groups, Kruskal-Wallis's test was used for non-parametric data, and One-Way-ANOVA test was used for parametric data. For three or more variables analysis, Two-Way-ANOVA test was used. Between each ANOVA test, Multivariant test analysis was used to compare each bidirectional comparison between single groups (Dunn´s test for the non-parametric Kruskal-Wallis multivariant analysis, Holm-Sidak´s test for the parametric One-Way ANOVA multivariant analysis, Bonferroni´s test for Two-Way ANOVA multivariant analysis). For correlations, non-parametric Spearman test was used. Outliers were discarded when were significant for the Grubb's test.

**Disclosure Statement and conflict of interest**

PP and JJMG declare that they are inventors in a patent filed on March 2020 by the Fundación para la Formación e Investigación Sanitaria de la Región de Murcia (PCT/EP2020/056729) for a method to identify NLRP3-immunocompromised septic patients. PP, JJMG and ABM are co-founders of Viva in vitro diagnostics SL, but declare that the research was conducted in the absence of any commercial or financial relationships that could be construed as a potential conflict of interest. The remaining authors declare no competing interests.

**Funding**

This work was supported by grants from MCIN/AEI/10.13039/501100011033 and European Union «Next Generation EU/PRTR» (grants PID2020-116709RB-I00, CNS2022-135105, PID2023-147531OB-I00 and RED2022-134511-T to PP), the Instituto Salud Carlos III (grant AC22/00009 to PP) and the Fundación Séneca (grant grant 21897/PI/22 to PP and 21967/JLI/22 to JJMG). JJGM was supported by a Maria Zambrano fellowship at University of Murcia. AG was supported by an FPI doctoral fellowship from *Ministerio de Ciencia, Innovación y Universidades* (PRE2021-100356). SVM was supported by a fellowship from Instituto Salud Carlos III (FI21/00073). CM-L was funded by the fellowship PRE2018-086824 (Ministerio economía y competitividad). LH-N was supported by the fellowship 21214/FPI/19 (Fundación Séneca, Región de Murcia, Spain).

**Acknowledgements**

We thank A Gomez for cell culture and lab assistance, and the members of Dr. Pelegrin's laboratory for all comments and suggestions. We also acknowledge to the animal facility from the University of Murcia, as well as the SPF-animal house, Pathology, Genomics and Bioinformatics platforms from the Pascual Parrilla-Biomedical Research Institute of Murcia (IMIB-PP).

**Authors Contribution**

JJMG visualized and administered the research. JJMG and PP conceptualized, provided funding, and wrote the manuscript. JJMG and SR did the formal analysis, wrote, and edited the manuscript. ABM provided funding. JJMG, AG, IQR, SVM. CML and LHN performed the experimental research.

528 REFERENCES


529 1. Medzhitov R. Origin and physiological roles of inflammation. *Nature* **(2008)** 454:428–435.
530 doi: 10.1038/nature07201

531 2. Sharma D, Kanneganti T-D. The cell biology of inflammasomes: Mechanisms of
532 inflammasome activation and regulation. *Journal of Cell Biology* **(2016)** 213:617–629. doi:
533 10.1083/jcb.201602089

534 3. Tartey S, Kanneganti T. Differential role of the NLRP3 inflammasome in infection and
535 tumorigenesis. *Immunology* **(2019)** 156:329–338. doi: 10.1111/imm.13046

536 4. Akira S, Uematsu S, Takeuchi O. Pathogen Recognition and Innate Immunity. *Cell* **(2006)**
537 124:783–801. doi: 10.1016/j.cell.2006.02.015

538 5. Martinon F, Burns K, Tschopp J. The Inflammasome: a molecular platform triggering
539 activation of inflammatory caspases and processing of proIL-beta. *Mol Cell* **(2002)** 10:417–
540 426. doi: 10.1016/S1097-2765(02)00599-3

541 6. Shi J, Zhao Y, Wang K, Shi X, Wang Y, Huang H, Zhuang Y, Cai T, Wang F, Shao F.
542 Cleavage of GSDMD by inflammatory caspases determines pyroptotic cell death. *Nature*
543 **(2015)** 526:660–665. doi: 10.1038/nature15514

544 7. Kayagaki N, Kornfeld OS, Lee BL, Stowe IB, O'Rourke K, Li Q, Sandoval W, Yan D,
545 Kang J, Xu M, et al. NINJ1 mediates plasma membrane rupture during lytic cell death.
546 *Nature* **(2021)** 591:131–136. doi: 10.1038/s41586-021-03218-7

547 8. Losa M, Emmenegger M, De Rossi P, Schürch PM, Serdiuk T, Pengo N, Capron D, Bieli
548 D, Bargenda N, Rupp NJ, et al. The ASC inflammasome adapter governs SAA-derived
549 protein aggregation in inflammatory amyloidosis. *EMBO Mol Med* **(2024)** 16:2024–2042.
550 doi: 10.1038/s44321-024-00107-0

551 9. Baroja-Mazo A, Martín-Sánchez F, Gomez AI, Martínez CM, Amores-Iniesta J, Compan
552 V, Barberà-Cremades M, Yagüe J, Ruiz-Ortiz E, Antón J, et al. The NLRP3 inflammasome
553 is released as a particulate danger signal that amplifies the inflammatory response. *Nat*
554 *Immunol* **(2014)** 15:738–748. doi: 10.1038/ni.2919

555 10. Alarcón-Vila C, Hurtado-Navarro L, Mateo S V, Peñín-Franch A, Martínez CM, Molina-
556 López C, Baños MC, Gómez AI, Gómez-Román J, Baroja-Mazo A, et al. The
557 inflammasome adaptor protein ASC promotes amyloid deposition in cryopyrin-associated
558 periodic syndromes. *EMBO Mol Med* **(2024)** 17:41–53. doi: 10.1038/s44321-024-00176-1

559 11. Bertheloot D, Wanderley CW, Schneider AH, Schiffelers LD, Wuerth JD, Tödtmann JM,
560 Maasewerd S, Hawwari I, Duthie F, Rohland C, et al. Nanobodies dismantle post-pyroptotic
561 ASC specks and counteract inflammation *in vivo*. *EMBO Mol Med* **(2022)** 14: doi:
562 10.15252/emmm.202115415
563 12. Venegas C, Kumar S, Franklin BS, Dierkes T, Brinkschulte R, Tejera D, Vieira-Saecker A,
564 Schwartz S, Santarelli F, Kummer MP, et al. Microglia-derived ASC specks cross-seed
565 amyloid-β in Alzheimer's disease. *Nature* **(2017)** 552:355–361. doi: 10.1038/nature25158
566 13. Franklin BS, Bossaller L, De Nardo D, Ratter JM, Stutz A, Engels G, Brenker C, Nordhoff
567 M, Mirandola SR, Al-Amoudi A, et al. The adaptor ASC has extracellular and "prionoid"
568 activities that propagate inflammation. *Nat Immunol* **(2014)** 15:727–737. doi:
569 10.1038/ni.2913
570 14. Henry LP, Bruijning M, Forsberg SKG, Ayroles JF. The microbiome extends host
571 evolutionary potential. *Nat Commun* **(2021)** 12:5141. doi: 10.1038/s41467-021-25315-x
572 15. Kudelka MR, Stowell SR, Cummings RD, Neish AS. Intestinal epithelial glycosylation in
573 homeostasis and gut microbiota interactions in IBD. *Nat Rev Gastroenterol Hepatol* **(2020)**
574 17:597–617. doi: 10.1038/s41575-020-0331-7
575 16. Muller PA, Matheis F, Schneeberger M, Kerner Z, Jové V, Mucida D. Microbiota-
576 modulated CART+ enteric neurons autonomously regulate blood glucose. *Science* **(2020)**
577 370:314–321. doi: 10.1126/science.abd6176
578 17. Seo S-U, Kamada N, Muñoz-Planillo R, Kim Y-G, Kim D, Koizumi Y, Hasegawa M,
579 Himpsl SD, Browne HP, Lawley TD, et al. Distinct Commensals Induce Interleukin-1β via
580 NLRP3 Inflammasome in Inflammatory Monocytes to Promote Intestinal Inflammation in
581 Response to Injury. *Immunity* **(2015)** 42:744–755. doi: 10.1016/j.immuni.2015.03.004
582 18. Feng Y, Huang Y, Wang Y, Wang P, Song H, Wang F. Antibiotics induced intestinal tight
583 junction barrier dysfunction is associated with microbiota dysbiosis, activated NLRP3
584 inflammasome and autophagy. *PLoS One* **(2019)** 14:e0218384. doi:
585 10.1371/journal.pone.0218384
586 19. Sokolova M, Yang K, Hansen SH, Louwe MC, Kummen M, Hov JER, Sjaastad I, Berge
587 RK, Halvorsen B, Aukrust P, et al. NLRP3 inflammasome deficiency attenuates metabolic
588 disturbances involving alterations in the gut microbial profile in mice exposed to high fat
589 diet. *Sci Rep* **(2020)** 10:21006. doi: 10.1038/s41598-020-76497-1

590 20. Finucane OM, Lyons CL, Murphy AM, Reynolds CM, Klinger R, Healy NP, Cooke AA,
591 Coll RC, McAllan L, Nilaweera KN, et al. Monounsaturated Fatty Acid–Enriched High-Fat
592 Diets Impede Adipose NLRP3 Inflammasome–Mediated IL-1β Secretion and Insulin
593 Resistance Despite Obesity. *Diabetes* **(2015)** 64:2116–2128. doi: 10.2337/db14-1098
594 21. Levy M, Thaiss CA, Zeevi D, Dohnalová L, Zilberman-Schapira G, Mahdi JA, David E,
595 Savidor A, Korem T, Herzig Y, et al. Microbiota-Modulated Metabolites Shape the
596 Intestinal Microenvironment by Regulating NLRP6 Inflammasome Signaling. *Cell* **(2015)**
597 163:1428–1443. doi: 10.1016/j.cell.2015.10.048
598 22. Zhang J, Yu Q, Jiang D, Yu K, Yu W, Chi Z, Chen S, Li M, Yang D, Wang Z, et al.
599 Epithelial Gasdermin D shapes the host-microbial interface by driving mucus layer
600 formation. *Sci Immunol* **(2022)** 7: doi: 10.1126/sciimmunol.abk2092
601 23. Miao P, Ruiqing T, Yanrong L, Zhuwen S, Huan Y, Qiong W, Yongnian L, Chao S.
602 Pyroptosis: A possible link between obesity-related inflammation and inflammatory
603 diseases. *J Cell Physiol* **(2022)** 237:1245–1265. doi: 10.1002/jcp.30627
604 24. Opoku E, Traughber CA, Zhang D, Iacano AJ, Khan M, Han J, Smith JD, Gulshan K.
605 Gasdermin D Mediates Inflammation-Induced Defects in Reverse Cholesterol Transport
606 and Promotes Atherosclerosis. *Front Cell Dev Biol* **(2021)** 9: doi:
607 10.3389/fcell.2021.715211
608 25. Xu B, Jiang M, Chu Y, Wang W, Chen D, Li X, Zhang Z, Zhang D, Fan D, Nie Y, et al.
609 Gasdermin D plays a key role as a pyroptosis executor of non-alcoholic steatohepatitis in
610 humans and mice. *J Hepatol* **(2018)** 68:773–782. doi: 10.1016/j.jhep.2017.11.040
611 26. Ahmad F, Mishra N, Ahrenstorf G, Franklin BS, Latz E, Schmidt RE, Bossaller L. Evidence
612 of inflammasome activation and formation of monocyte-derived ASC specks in HIV-1
613 positive patients. *AIDS* **(2018)** 32:299–307. doi: 10.1097/QAD.0000000000001693
614 27. Eckel RH, Grundy SM, Zimmet PZ. The metabolic syndrome. *The Lancet* **(2005)**
615 365:1415–1428. doi: 10.1016/S0140-6736(05)66378-7
616 28. Hamblin PS, Russell AW, Talic S, Zoungas S. The growing range of complications of
617 diabetes mellitus. *Trends in Endocrinology & Metabolism* **(2025)** doi:
618 10.1016/j.tem.2024.12.006
619 29. Oami T, Abtahi S, Shimazui T, Chen C-W, Sweat YY, Liang Z, Burd EM, Farris AB,
620 Roland JT, Tsukita S, et al. Claudin-2 upregulation enhances intestinal permeability,

621 immune activation, dysbiosis, and mortality in sepsis. *Proceedings of the National Academy*
622 *of Sciences* **(2024)** 121: doi: 10.1073/pnas.2217877121
623 30. Honda M, Kadohisa M, Yoshii D, Komohara Y, Hibi T. Directly recruited
624 GATA6 + peritoneal cavity macrophages contribute to the repair of intestinal serosal injury.
625 *Nat Commun* **(2021)** 12:7294. doi: 10.1038/s41467-021-27614-9
626 31. Markovich Z, Abreu A, Sheng Y, Han SM, Xiao R. Deciphering internal and external
627 factors influencing intestinal junctional complexes. *Gut Microbes* **(2024)** 16: doi:
628 10.1080/19490976.2024.2389320
629 32. Greer RL, Dong X, Moraes ACF, Zielke RA, Fernandes GR, Peremyslova E, Vasquez-
630 Perez S, Schoenborn AA, Gomes EP, Pereira AC, et al. Akkermansia muciniphila mediates
631 negative effects of IFNγ on glucose metabolism. *Nat Commun* **(2016)** 7:13329. doi:
632 10.1038/ncomms13329
633 33. Geach T. Mucin-munching bacteria modulate glucose metabolism. *Nat Rev Endocrinol*
634 **(2017)** 13:66–66. doi: 10.1038/nrendo.2016.201
635 34. Matsumoto H, Shiotani A, Katsumata R, Fukushima S, Handa Y, Osawa M, Murao T,
636 Handa O, Umegaki E, Inoue R, et al. Mucosa-Associated Microbiota in Patients with
637 Irritable Bowel Syndrome: A Comparison of Subtypes. *Digestion* **(2021)** 102:49–56. doi:
638 10.1159/000512167
639 35. Brooks JF, Behrendt CL, Ruhn KA, Lee S, Raj P, Takahashi JS, Hooper L V. The
640 microbiota coordinates diurnal rhythms in innate immunity with the circadian clock. *Cell*
641 **(2021)** 184:4154-4167.e12. doi: 10.1016/j.cell.2021.07.001
642 36. Matsuzawa M, Ando T, Fukase S, Kimura M, Kume Y, Ide T, Izawa K, Kaitani A, Hara M,
643 Nakamura E, et al. The protective role of conjunctival goblet cell mucin sialylation. *Nat*
644 *Commun* **(2023)** 14:1417. doi: 10.1038/s41467-023-37101-y
645 37. Yu K, Li Q, Sun X, Peng X, Tang Q, Chu H, Zhou L, Wang B, Zhou Z, Deng X, et al.
646 Bacterial indole-3-lactic acid affects epithelium–macrophage crosstalk to regulate intestinal
647 homeostasis. *Proceedings of the National Academy of Sciences* **(2023)** 120: doi:
648 10.1073/pnas.2309032120
649 38. Tirado-Hurtado I, Fajardo W, Pinto JA. DNA Damage Inducible Transcript 4 Gene: The
650 Switch of the Metabolism as Potential Target in Cancer. *Front Oncol* **(2018)** 8: doi:
651 10.3389/fonc.2018.00106

652 39. Luo Z-H, Niu M-W, Gong S-H, Wu G-Y, Wang T, Wang F-Z, Wei G-Q, He Z-K, Jiang Y,
653 Chen P. Intestinal epithelial chemokine (C-C motif) ligand 7 overexpression protects
654 against high fat diet-induced obesity and hepatic steatosis in mice. *Chin Med J (Engl)* **(2020)**
655 133:1805–1814. doi: 10.1097/CM9.0000000000000915
656 40. Merino B, Fernández-Díaz CM, Parrado-Fernández C, González-Casimiro CM, Postigo-
657 Casado T, Lobatón CD, Leissring MA, Cózar-Castellano I, Perdomo G. Hepatic insulin-
658 degrading enzyme regulates glucose and insulin homeostasis in diet-induced obese mice.
659 *Metabolism* **(2020)** 113:154352. doi: 10.1016/j.metabol.2020.154352
660 41. Su Q, Huang J, Chen X, Wang Y, Shao M, Yan H, Chen C, Ren H, Zhang F, Ni Y, et al.
661 Long-Term High-Fat Diet Decreases Renal Insulin-Degrading Enzyme Expression and
662 Function by Inhibiting the PPARγ Pathway. *Mol Nutr Food Res* **(2023)** 67: doi:
663 10.1002/mnfr.202200589
664 42. Bauer C, Duewell P, Mayer C, Lehr HA, Fitzgerald KA, Dauer M, Tschopp J, Endres S,
665 Latz E, Schnurr M. Colitis induced in mice with dextran sulfate sodium (DSS) is mediated
666 by the NLRP3 inflammasome. *Gut* **(2010)** 59:1192–1199. doi: 10.1136/gut.2009.197822
667 43. Frühbeck G, Gómez-Ambrosi J, Ramírez B, Becerril S, Rodríguez A, Mentxaka A, Valentí
668 V, Moncada R, Reina G, Baixauli J, et al. Decreased expression of the NLRP6
669 inflammasome is associated with increased intestinal permeability and inflammation in
670 obesity with type 2 diabetes. *Cellular and Molecular Life Sciences* **(2024)** 81:77. doi:
671 10.1007/s00018-024-05124-3
672 44. Tye H, Yu C-H, Simms LA, de Zoete MR, Kim ML, Zakrzewski M, Penington JS, Harapas
673 CR, Souza-Fonseca-Guimaraes F, Wockner LF, et al. NLRP1 restricts butyrate producing
674 commensals to exacerbate inflammatory bowel disease. *Nat Commun* **(2018)** 9:3728. doi:
675 10.1038/s41467-018-06125-0
676 45. Mullins B, Chen J. NLRP9 in innate immunity and inflammation. *Immunology* **(2021)**
677 162:262–267. doi: 10.1111/imm.13290
678 46. Patel S, Das A, Meshram P, Sharma A, Chowdhury A, Jariyal H, Datta A, Sarmah D, Nalla
679 LV, Sahu B, et al. Pyruvate kinase M2 in chronic inflammations: a potpourri of crucial
680 protein–protein interactions. *Cell Biol Toxicol* **(2021)** 37:653–678. doi: 10.1007/s10565-
681 021-09605-0

682 47. Palsson-McDermott EM, Curtis AM, Goel G, Lauterbach MAR, Sheedy FJ, Gleeson LE,
683 van den Bosch MWM, Quinn SR, Domingo-Fernandez R, Johnston DGW, et al. Pyruvate
684 Kinase M2 Regulates Hif-1α Activity and IL-1β Induction and Is a Critical Determinant of
685 the Warburg Effect in LPS-Activated Macrophages. *Cell Metab* **(2015)** 21:347. doi:
686 10.1016/j.cmet.2015.01.017
687 48. Sunny NE, Bril F, Cusi K. Mitochondrial Adaptation in Nonalcoholic Fatty Liver Disease:
688 Novel Mechanisms and Treatment Strategies. *Trends in Endocrinology & Metabolism*
689 **(2017)** 28:250–260. doi: 10.1016/j.tem.2016.11.006
690 49. Love MI, Huber W, Anders S. Moderated estimation of fold change and dispersion for
691 RNA-seq data with DESeq2. *Genome Biol* **(2014)** 15:550. doi: 10.1186/s13059-014-0550-
692 8
693 50. Kolde R. pheatmap: Pretty Heatmaps. *CRAN: Contributed Packages* **(2019)** doi:
694 10.32614/CRAN.package.pheatmap
695 51. Carlson M. Genome wide annotation for Mouse, primarily based on mapping using Entrez
696 Gene identifiers. *Bioconductor Package Maintainer* **(2023)**
697 52. Wickham H. *ggplot2: Elegant Graphics for Data Analysis.* 2nd edition. Springer. **(2016).**
698 53. McMurdie PJ, Holmes S. phyloseq: An R Package for Reproducible Interactive Analysis
699 and Graphics of Microbiome Census Data. *PLoS One* **(2013)** 8:e61217. doi:
700 10.1371/journal.pone.0061217
701
702

703 **Figure legends**

704 **Figure 1. ASC deficiency prevents gain of weight and glucose intolerance during high fat**
705 **diet.**

706 **A.** Body weight from *Pycard*$^{+/+}$ (blue, n=4), *Pycard*$^{-/-}$ (green, n=2) mice fed with a normal chow
707 diet (NCD).

708 **B.** Body weight from *Pycard*$^{+/+}$ (red, n=5), *Pycard*$^{-/-}$ (green, n=4), and *Pycard*$^{-/-}$ with intraperitoneal
709 injection of recombinant ASC oligomers (+ipASC) (purple, n=5) mice fed with a high fat diet
710 (HFD).

711 **C,D.** Glucose tolerance on mice at 3 months **(C)** and 5 months **(D)** of NCD or HFD.

712 Each dot represents a distinct animal, bars represent the mean, error bars represent SEM. Two-
713 way ANOVA together multivariant Bonferroni's test was used for **A-D** (*p≤0.05; **p≤0.01; ***
714 p≤0.001).

715

716 **Figure 2. ASC-deficiency reduces intestinal permeability and increases peritoneal cell**
717 **infiltration in high-fat-diet.**

718 **A,B.** FITC-dextran concentration in plasma of *Pycard*$^{+/+}$or *Pycard*$^{-/-}$ mice fed with a normal chow
719 diet (NCD) or high fat diet (HFD) for 5 months; *Pycar*$^{-/-}$ mice with intraperitoneal injection of
720 recombinant ASC oligomers (+ipASC).

721 **C,D**. Number of peritoneal cells of mice treated as in A,B.

722 **E,F.** Correlation between FITC-dextran plasma concentration and peritoneal cells of mice treated
723 as in A,B.

724 **G,H.** IL-1β release from peritoneal cells collected from mice treated as in as in A,B and then *in*
725 *vitro* stimulated as described in the legend.

726 *Pycard*$^{+/+}$mice fed with NCD (n=4) in comparison with HFD (n= 5) **(A, C, E, G)**, and on HFD fed
727 ASC$^{+/+}$ (n=4-8) in comparison with *Pycard*$^{-/-}$ mice with (n=5) or without ipASC (n=4) **(B, D, F,**
728 **H)**.

729 Each dot represents a distinct animal, bars represent the mean, error bars represent SEM. *t*-student
730 test was used for **A**. One-way ANOVA and multivariant Holm-Sidak´s test was done for **B**. Mann-
731 Whitney's test was done for **C**. Kruskal Wallis and multivariant Dunn's test was used for **D**.
732 Spearman's correlation test was used for **E, F**. Two-way ANOVA and multivariant Bonferroni test
733 was used for **G, H** (ns, p>0,05; *p≤0.05; **p≤0.01; *** p≤0.001).

734

735 **Figure 3. Extracellular ASC oligomers modulates microbiota biodiversity during high-fat-**
736 **diet.**

737 **A-D.** Relative microbiota abundance species **(A)** or class levels **(B-D)** on high fat diet (HFD) fed
738 for 5 months *Pycard*$^{+/+}$ (n=5) **(A, B)**, *Pycard*$^{-/-}$ mice (n=5) **(A, C),** or *Pycard*$^{-/-}$ mice with
739 intraperitoneal injection of recombinant ASC oligomers (ipASC) (n=4) **(A, D)**.

740 **E-H**. Relative abundance of *Akkermansia* **(E)**, *Bacteroides* **(F)**, *Enteractinococcus* **(G)**, and
741 *Atopostipes* **(H)** in the same conditions as in A-D.

742 Each dot represents a distinct animal, bars represent the mean, error bars represent SEM. One-way
743 ANOVA together multivariant Holm-Sidak's test was used for **E, F**. Kruskal-Wallis together
744 multivariant Dunn's test was done for **G, H** (**$p \leq 0.01$).

745

746 **Figure 4. ASC induces bacteria attachment in small intestinal *villi* during high-fat-diet and**
747 **alters epithelial integrity-related genes and increase innate immune response.**

748 **A,B,C.** Hematoxilin and eosin histology of the small intestine of mice fed with a high fat diet
749 (HFD) for 5 months, *Pycard*$^{+/+}$ (**A**), *Pycard*$^{-/-}$ mice (**B**), or *Pycard*$^{-/-}$ mice with intraperitoneal
750 injection of recombinant ASC oligomers (ipASC) **(C)**. Scale bar = 200 μm.

751 **D**, Differential expressed genes in the small intestine of mice treated as in A-C.

752 **E**, Gene Ontology differential expressed pathways in the small intestine of mice treated as in A,B.

753 **F,** Interleukin (IL)-1β detection in the small intestine of mice treated as in A-C
754 *Pycard*$^{+/+}$ (n=3-5), *Pycard*$^{-/-}$ mice (n=3), *Pycard*$^{-/-}$ mice with intraperitoneal injection of
755 recombinant ASC oligomers (ipASC) (n=5).

756 Black arrows indicate presence of bacteria in **(A)**, blue arrows indicate presence of mucus in **(B)**,
757 red arrows indicate absence of mucus in **(C)**.

758 Each dot represents a distinct animal, bars represent the mean, error bars represent SEM. One Way
759 ANOVA together multivariant Holm-Sidak's test was used for **F.** (*$p \leq 0.05$).

760

761 **Figure 5. ASC deficiency increase glycolytic and tricarboxylic acids related genes in high-**
762 **fat-diet.**

763 **A-F.** Relative mRNA expression of *Pkm2* **(A)**, *Ldha* **(B)**, *Pdha* **(C)**, *Glud1* **(D)**, *Sdha* **(E)**, and
764 *Cpt1a* **(F)** on the small intestine of mice fed with a HFD.

765 *Pycard*$^{+/+}$ (n=5), *Pycard*$^{-/-}$ mice (n=4) or *Pycard*$^{-/-}$ mice with intraperitoneal injection of
766 recombinant ASC oligomers (ipASC) (n=5).
767 Bars represent the mean, error bars represent SEM. Kruskal Wallis together multivariant Dunn's
768 test was used for all panels (*p≤0.05; **p≤0.01).
769
770 **Figure 6. ASC deficiency enhance hepatic metabolism under high-fat-diet and reduce**
771 **steatosis.**
772 **A-C.** Haematoxylin and eosin histology of the liver of mice fed with a high fat diet (HFD) for 5
773 months, *Pycard*$^{+/+}$ (**A**), *Pycard*$^{-/-}$ mice (**B**), or *Pycard*$^{-/-}$ mice with intraperitoneal injection of
774 recombinant ASC oligomers (ipASC) **(C)**. Scale bar = 200 μm.
775 **D-H.** Relative mRNA expression of *Pgc1a* **(D)***, Nnt* **(E)***, Glud1* **(F)***, Cyp7a1* **(G)***,* and *Shp* **(H)** in
776 the liver of mice treated as in C-D.
777 **I.** Interleukin (IL)-1β production in the liver of mice treated as in C-D.
778 HFD fed *Pycard*$^{+/+}$ (n=5), *Pycard*$^{-/-}$ mice (n=4), *Pycard*$^{-/-}$ mice with intraperitoneal injection of
779 recombinant ASC oligomers (ipASC) (n=5).
780 Each dot represents a distinct animal, bars represent the mean, error bars represent SEM. One way
781 ANOVA together multivariant Holm-Sidak's test was used for **(D-I)** (*p≤0.05; **p≤0.01; ***
782 p≤0.001).
783
784

785 **Supplemental information**

786 **Supplemental Figure 1. Body weight of different mice genotypes.**

787 **A.** Body weight on normal chow diet (NCD) fed *Pycard*$^{+/+}$ (blue, n=3), and *Pycard*$^{-/-}$ (green, n=2),
788 male mice, and on NCD fed wild type (blue, n=4), and *Pycard*$^{-/-}$ (green, n=2), female mice.

789 **B-C**. Body weight on *Pycard*$^{+/+}$mice fed with high fat diet (HFD) (n=3) in comparison with normal
790 chow diet fed (NCD) mice (n=4) **(B)**, and on HFD fed wild type in comparison with *Gsdmd*$^{-/-}$ **(C)**.
791 Values represent the mean of each condition and error bars represent SEM. Two-way ANOVA
792 together multivariant Bonferroni's test was used for all panels (*p≤0.05; **p≤0.01; *** p≤0.001).

793

794 **Supplemental Figure 2. Cytokines produced from peritoneal cells and intestinal permeability**
795 **in *Pycard*$^{-/-}$ mice in comparison with wild type mice.**

796 **A.** IL-1β release from peritoneal cells treated *in vitro* with the treatments indicated in the legend.
797 Peritoneal cells were isolated from normal chow diet (NCD) fed *Pycard*$^{-/-}$ (n=4) and *Pycard*$^{+/+}$
798 (n=4) mice.

799

800 **B,C.** IL-6 production on mice fed with high fat diet (HFD) for 5 months, *Pycard*$^{+/+}$ (n=5), *Pycard*$^{-}$
801 $^{/-}$ mice (n=4), *Pycard*$^{-/-}$ mice with intraperitoneal injection of recombinant ASC oligomers (ipASC)
802 (n=5) **(B)** and on wild type mice fed with NCD or HFD **(C)**..

803

804 Each dot represents a distinct animal, bars represent the mean, error bars represent SEM. Kruskal-
805 Wallis together multivariant Dunn's test was used for **A-C**. (*p≤0.05; **p≤0.01; *** p≤0.001).

806

807 **Supplemental Figure 3. Analysis of the intestinal microbiota of mice fed with normal chow**
808 **diet or high fat diet.**

809 **A-C.** Relative abundance of the total faecal microbiota at class level **(A, B)**, and of *Akkermansia*
810 **(C)** on *Pycard*$^{+/+}$mice fed with a normal chow diet (NCD) (n=4) in comparison with high fat diet
811 (HFD) (n= 5).

812 Each dot represents a distinct animal, bars represent the mean, error bars represent SEM. *t*-student
813 test was used for **C**.

814

815 **Supplemental Figure 4. Histological analysis of the small intestine from mice fed with normal**
816 **chow diet or with high fat diet.**
817 **A-B.** Haematoxylin and eosin histology of the small intestine of mice fed with a normal chow diet
818 (NCD) representative of n=4 **(A**), or a high fat diet (HFD) representative of n= 5 **(B)** for 5 months.
819 Scale bar = 200 μm.
820 **C-D.** Interleukin (IL)-6 production **(C),** mRNA relative expression of *Pycard* **(D),** and principal
821 components analysis **(E)** in the small intestine of mice fed with a HFD, *Pycard*$^{+/+}$ (n=4), *Pycard*$^{-/-}$
822 mice (n=4), *Pycard*$^{-/-}$ mice with intraperitoneal injection of recombinant ASC oligomers (ipASC)
823 (n=5).
824 Each dot represents a distinct animal, bars represent the mean, error bars represent SEM. One way
825 ANOVA together multivariant Holm-Sidak's test was used for **C**. Kruskal-Wallis together
826 multivariant Dunn's test was used for **D** (*** $p \leq 0.001$).
827
828 **Supplemental Figure 5. Histological analysis of the liver from mice fed with normal chow**
829 **diet compared with high fat diet.**
830 **A, B.** Haematoxylin and eosin histology of the liver of *Pycard*$^{+/+}$mice fed with a normal chow diet
831 (NCD) representative of n=4 **(A**), or a high fat diet (HFD) representative of n= 5 for 5 months **(B)**.
832 Scale bar = 200 μm.

# Figure 1

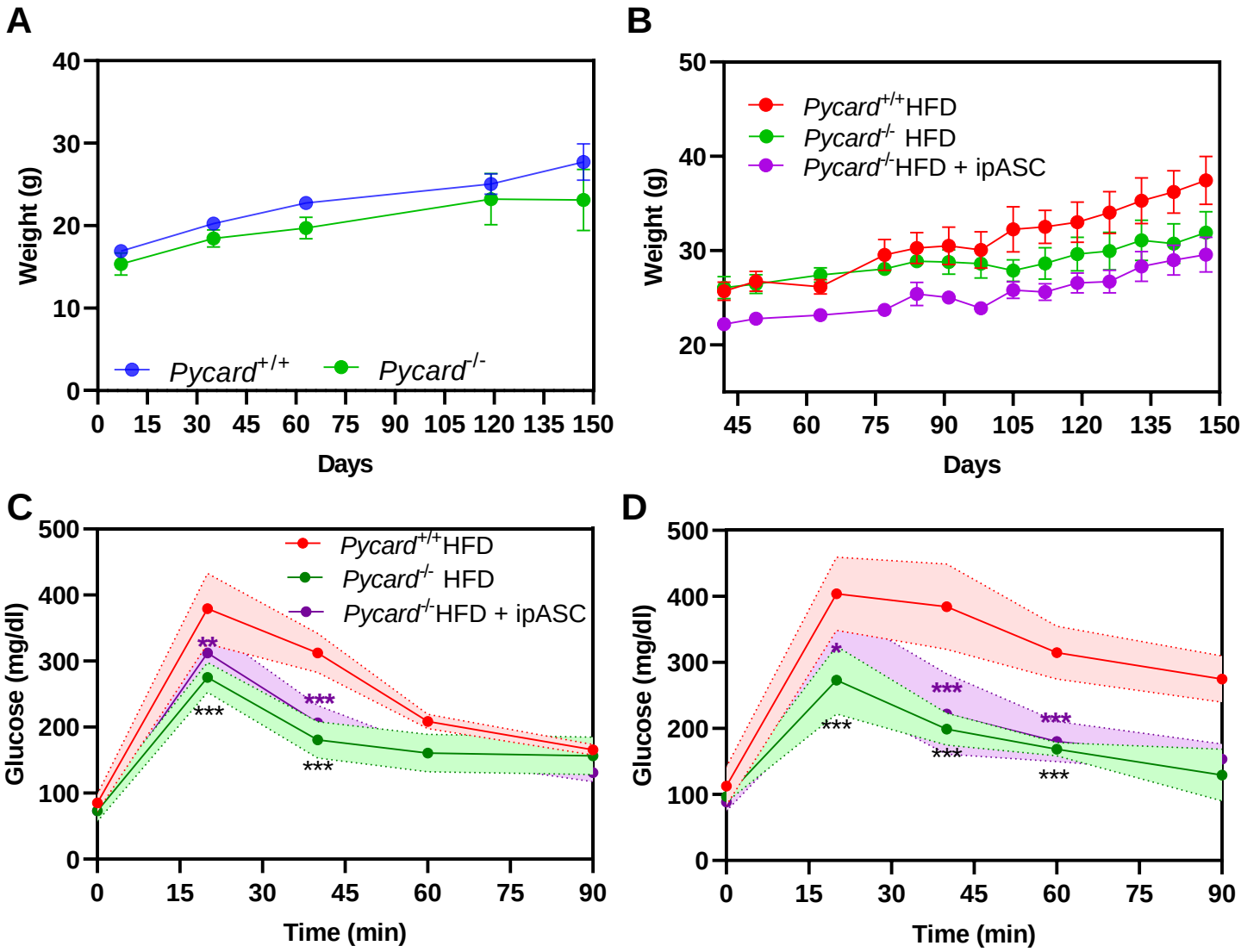
A
Weight (g)
Days
Pycard+/+
Pycard-/-
B
Weight (g)
Days
Pycard+/+HFD
Pycard-/- HFD
Pycard-/-HFD + ipASC
C
Glucose (mg/dl)
Time (min)
Pycard+/+HFD
Pycard-/- HFD
Pycard-/-HFD + ipASC
D
Glucose (mg/dl)
Time (min)

# Figure 2

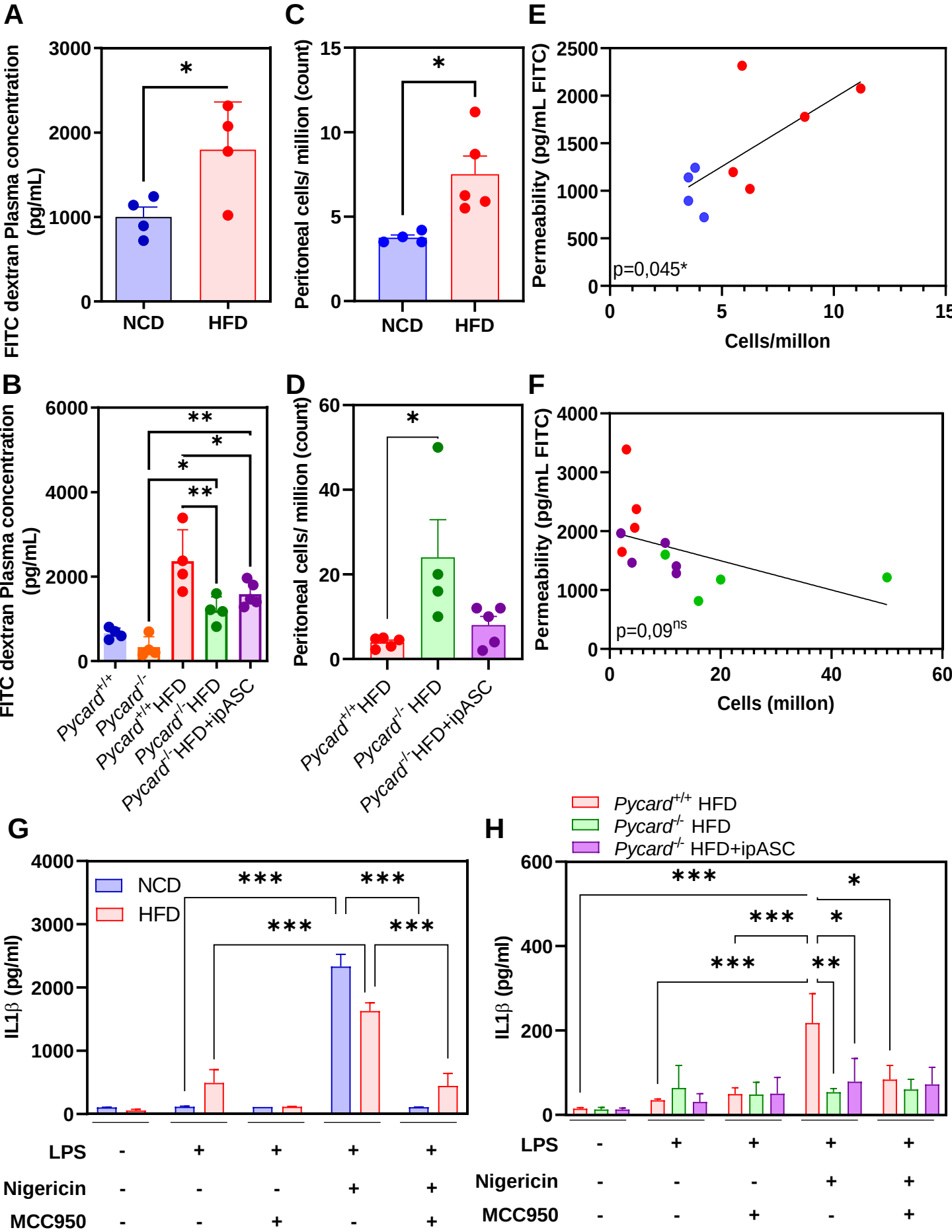
A
FITC dextran Plasma concentration (pg/mL)
3000
2000
1000
0
*
NCD
HFD
C
Peritoneal cells/ million (count)
15
10
5
0
*
NCD
HFD
E
Permeability (pg/mL FITC)
2500
2000
1500
1000
500
0
p=0,045*
0
5
10
15
Cells/millon
B
FITC dextran Plasma concentration (pg/mL)
6000
4000
2000
0
**
*
*
**
Pycard+/+
Pycard-/-
Pycard+/+HFD
Pycard-/-HFD
Pycard-/-HFD+ipASC
D
Peritoneal cells/ million (count)
60
40
20
0
*
Pycard+/+HFD
Pycard-/- HFD
Pycard-/-HFD+ipASC
F
Permeability (pg/mL FITC)
4000
3000
2000
1000
0
p=0,09ns
0
20
40
60
Cells (millon)
G
IL1β (pg/ml)
4000
3000
2000
1000
0
NCD
HFD
***
***
***
***
LPS - + + + +
Nigericin - - - + +
MCC950 - - + - +
H
Pycard+/+ HFD
Pycard-/- HFD
Pycard-/- HFD+ipASC
IL1β (pg/ml)
600
400
200
0
***
*
***
*
***
**
LPS - + + + +
Nigericin - - - + +
MCC950 - - + - +

# Figure 3

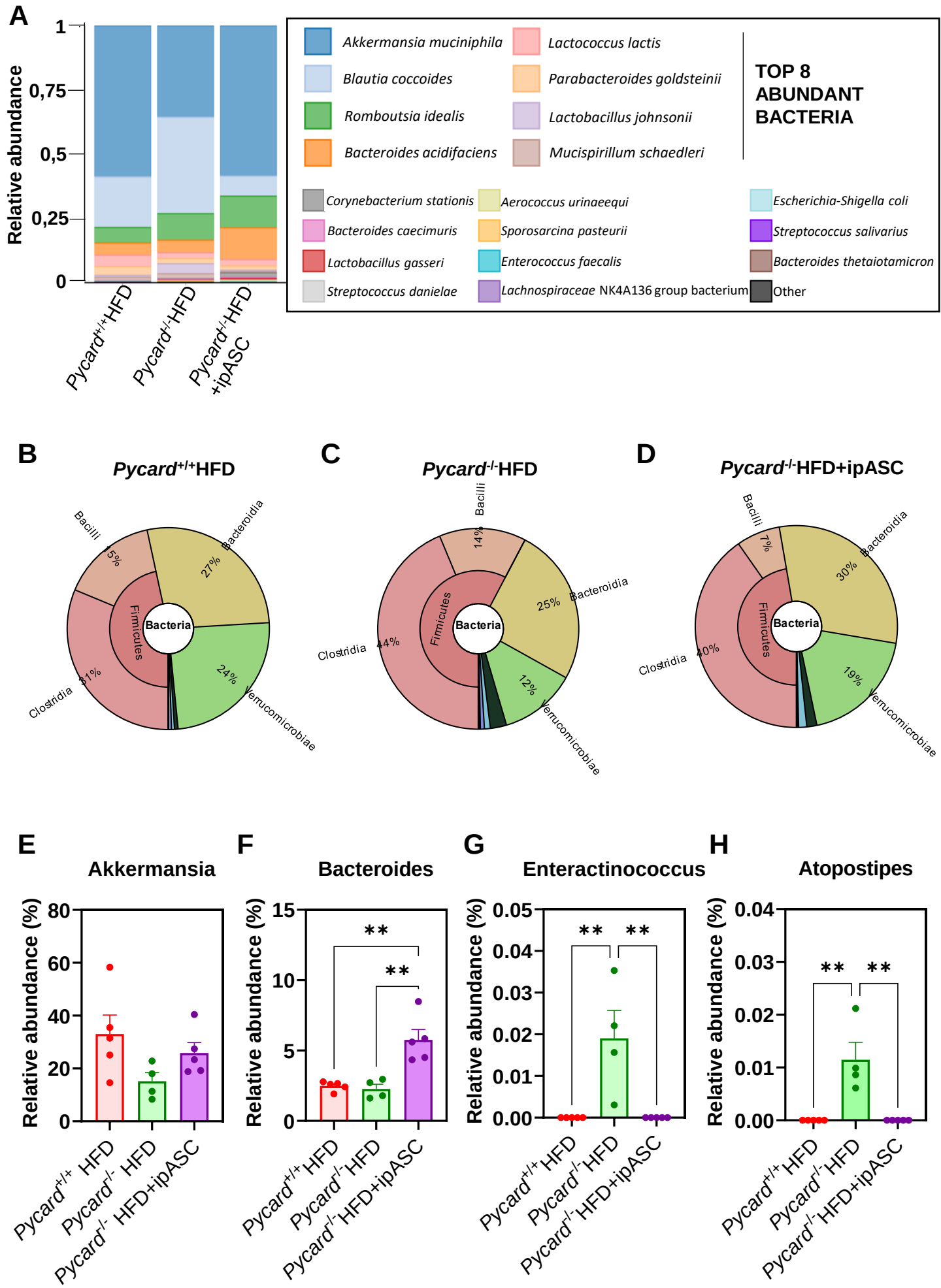
A
Relative abundance
1
0,75
0,5
0,25
0
Pycard+/+HFD
Pycard-/-HFD
Pycard-/-HFD +ipASC
Akkermansia muciniphila
Blautia coccoides
Romboutsia idealis
Bacteroides acidifaciens
Lactococcus lactis
Parabacteroides goldsteinii
Lactobacillus johnsonii
Mucispirillum schaedleri
TOP 8 ABUNDANT BACTERIA
Corynebacterium stationis
Bacteroides caecimuris
Lactobacillus gasseri
Streptococcus danielae
Aerococcus urinaeequi
Sporosarcina pasteurii
Enterococcus faecalis
Lachnospiraceae NK4A136 group bacterium
Escherichia-Shigella coli
Streptococcus salivarius
Bacteroides thetaiotamicron
Other
B
Pycard+/+HFD
Bacilli 5%
Bacteroidia 27%
Bacteria
Firmicutes
Clostridia 31%
24% Verrucomicrobiae
C
Pycard-/-HFD
Bacilli 14%
Bacteroidia 25%
Bacteria
Firmicutes
Clostridia 44%
12% Verrucomicrobiae
D
Pycard-/-HFD+ipASC
Bacilli 7%
Bacteroidia 30%
Bacteria
Firmicutes
Clostridia 40%
19% Verrucomicrobiae
E
Akkermansia
Relative abundance (%)
80
60
40
20
0
Pycard+/+ HFD
Pycard-/- HFD
Pycard-/- HFD+ipASC
F
Bacteroides
Relative abundance (%)
15
10
5
0
**
**
Pycard+/+HFD
Pycard-/-HFD
Pycard-/-HFD+ipASC
G
Enteractinococcus
Relative abundance (%)
0.05
0.04
0.03
0.02
0.01
0.00
** **
Pycard+/+HFD
Pycard-/-HFD
Pycard-/-HFD+ipASC
H
Atopostipes
Relative abundance (%)
0.04
0.03
0.02
0.01
0.00
** **
Pycard+/+HFD
Pycard-/-HFD
Pycard-/-HFD+ipASC

# Figure 4

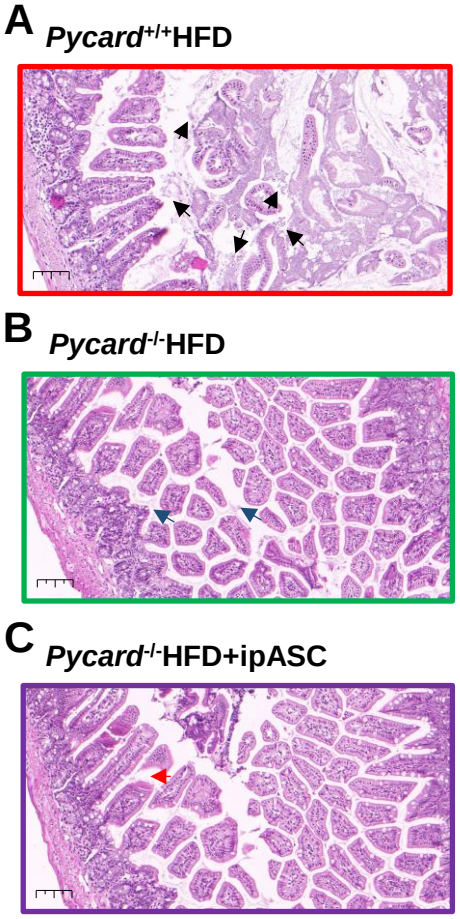
A
Pycard+/+HFD
B
Pycard-/-HFD
C
Pycard-/-HFD+ipASC

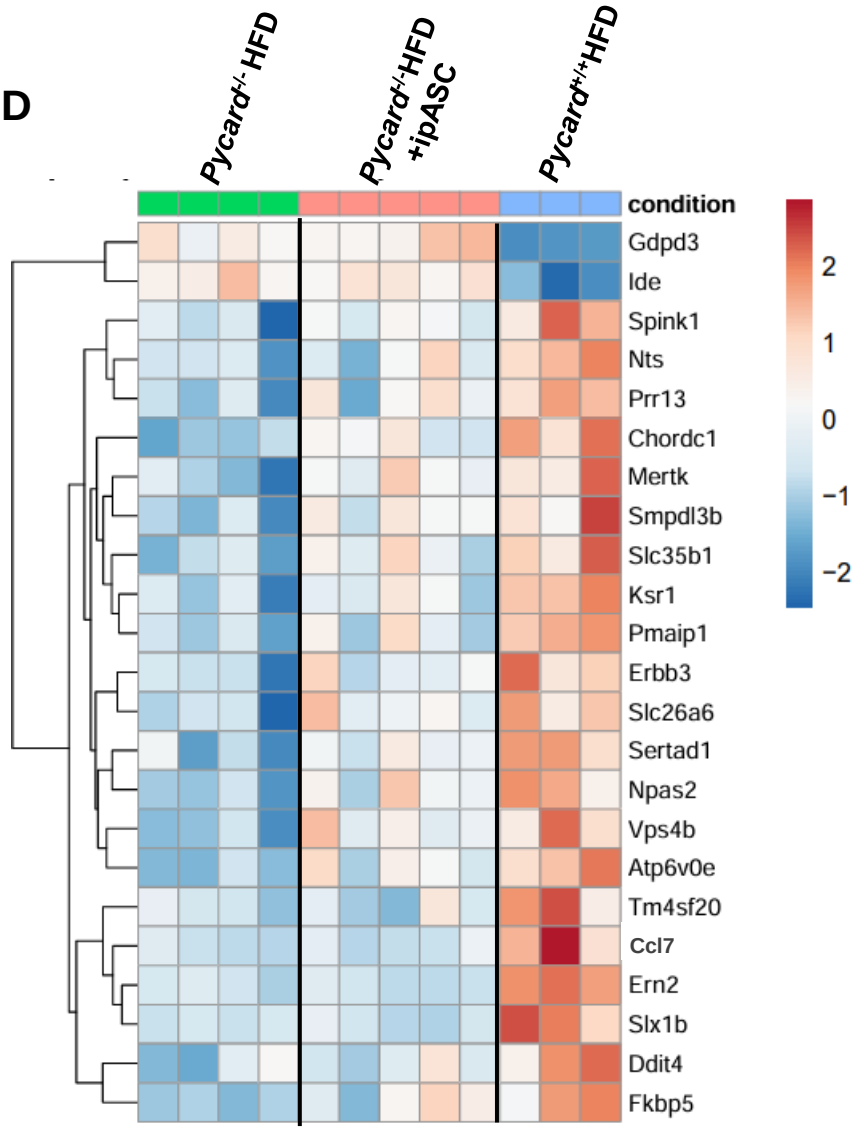
D
Pycard-/- HFD
Pycard-/-HFD +ipASC
Pycard+/+HFD
condition
Gdpd3
Ide
Spink1
Nts
Prr13
Chordc1
Mertk
Smpdl3b
Slc35b1
Ksr1
Pmaip1
Erbb3
Slc26a6
Sertad1
Npas2
Vps4b
Atp6v0e
Tm4sf20
Ccl7
Ern2
Slx1b
Ddit4
Fkbp5
2
1
0
−1
−2

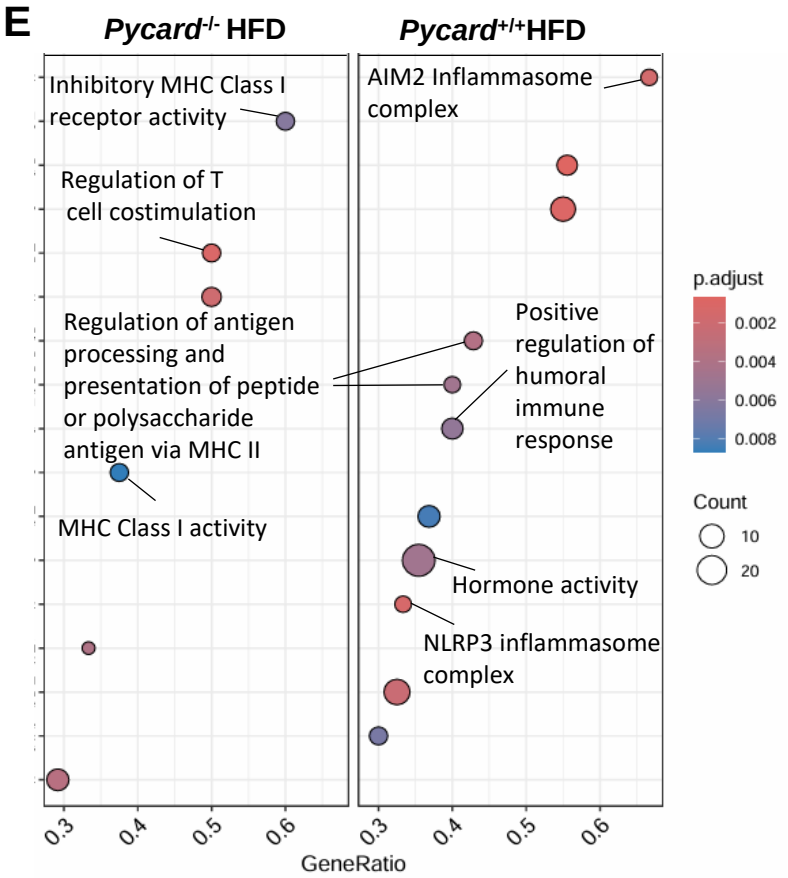
E
Pycard-/- HFD
Pycard+/+HFD
Inhibitory MHC Class I receptor activity
Regulation of T cell costimulation
Regulation of antigen processing and presentation of peptide or polysaccharide antigen via MHC II
MHC Class I activity
AIM2 Inflammasome complex
Positive regulation of humoral immune response
Hormone activity
NLRP3 inflammasome complex
p.adjust
0.002
0.004
0.006
0.008
Count
10
20
0.3
0.4
0.5
0.6
GeneRatio

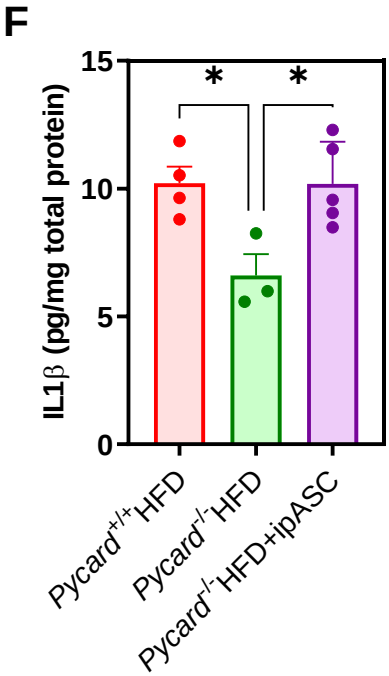
F
IL1β (pg/mg total protein)
15
10
5
0
*
*
Pycard+/+HFD
Pycard-/-HFD
Pycard-/-HFD+ipASC

# Figure 5

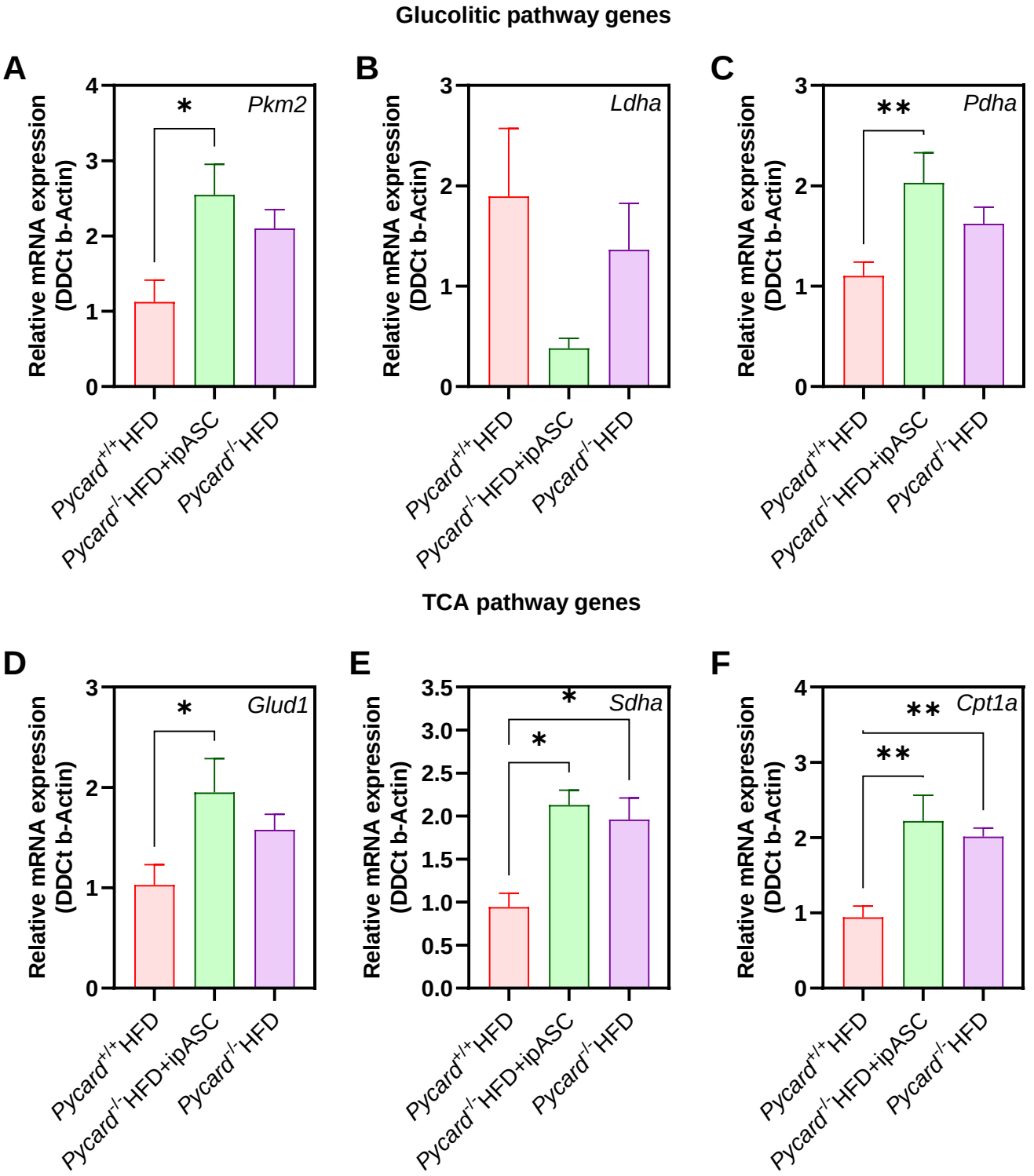
Glucolitic pathway genes
A
Pkm2
*
Relative mRNA expression (DDCt b-Actin)
0
1
2
3
4
Pycard+/+HFD
Pycard-/-HFD+ipASC
Pycard-/-HFD
B
Ldha
Relative mRNA expression (DDCt b-Actin)
0
1
2
3
Pycard+/+HFD
Pycard-/-HFD+ipASC
Pycard-/-HFD
C
Pdha
**
Relative mRNA expression (DDCt b-Actin)
0
1
2
3
Pycard+/+HFD
Pycard-/-HFD+ipASC
Pycard-/-HFD
TCA pathway genes
D
Glud1
*
Relative mRNA expression (DDCt b-Actin)
0
1
2
3
Pycard+/+HFD
Pycard-/-HFD+ipASC
Pycard-/-HFD
E
Sdha
*
*
Relative mRNA expression (DDCt b-Actin)
0.0
0.5
1.0
1.5
2.0
2.5
3.0
3.5
Pycard+/+HFD
Pycard-/-HFD+ipASC
Pycard-/-HFD
F
Cpt1a
**
**
Relative mRNA expression (DDCt b-Actin)
0
1
2
3
4
Pycard+/+HFD
Pycard-/-HFD+ipASC
Pycard-/-HFD

# Figure 6

A

*Pycard*$^{+/+}$ HFD

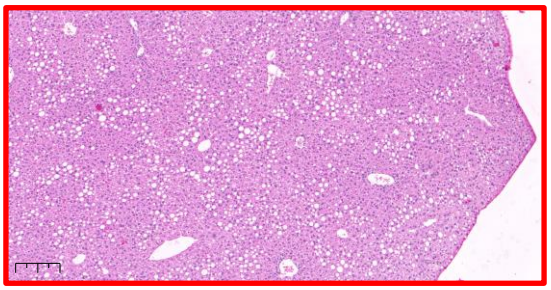

B

*Pycard*$^{-/-}$HFD

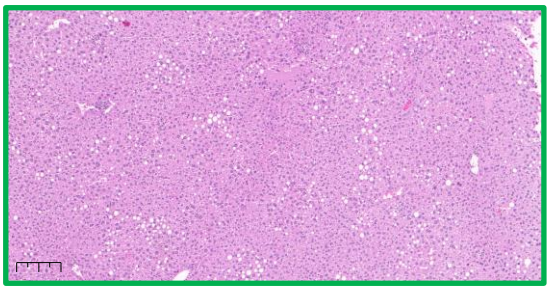

C

*Pycard*$^{-/-}$HFD+ipASC

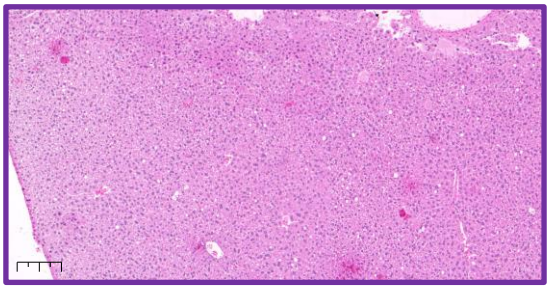

D

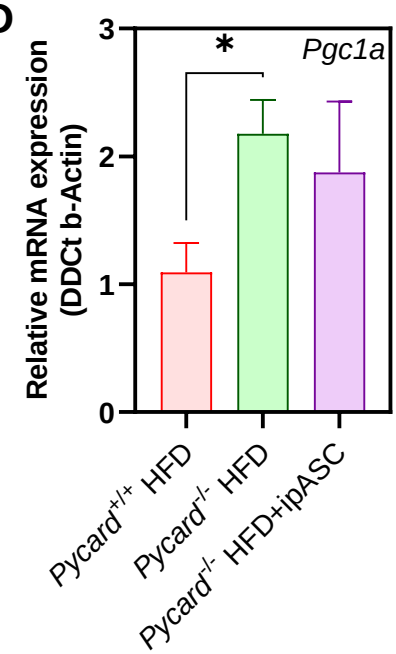


G

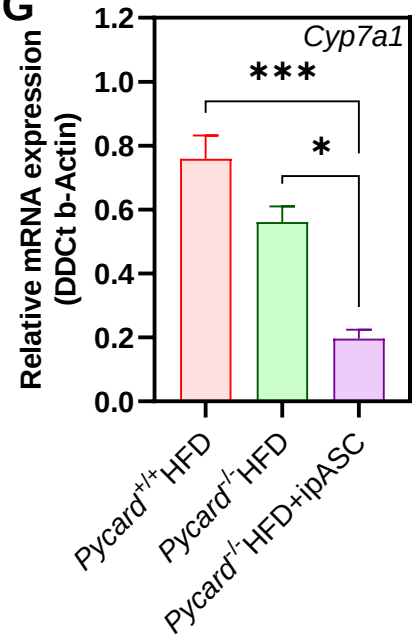


E

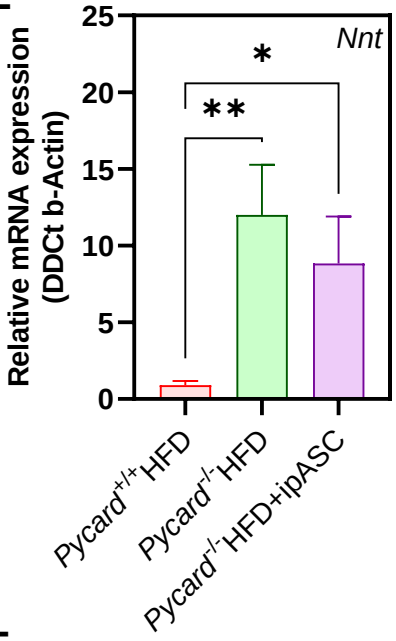


H

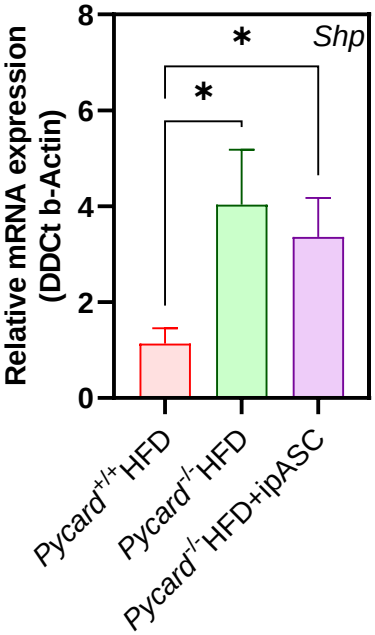


F

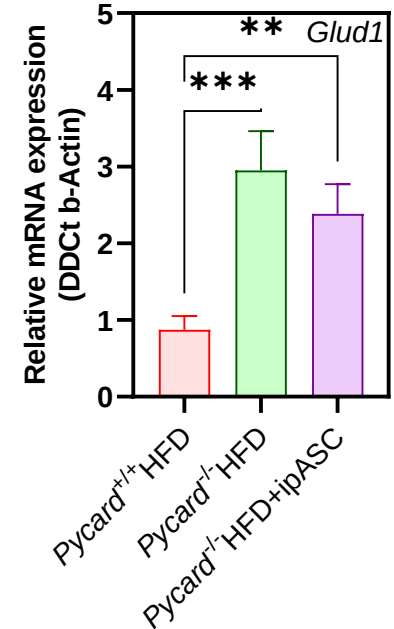


I

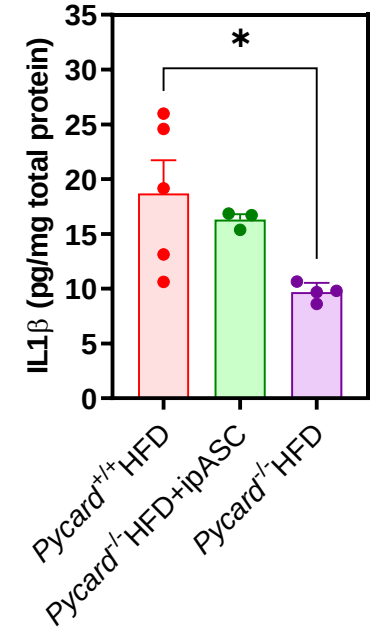

# Supplementary Figure 1

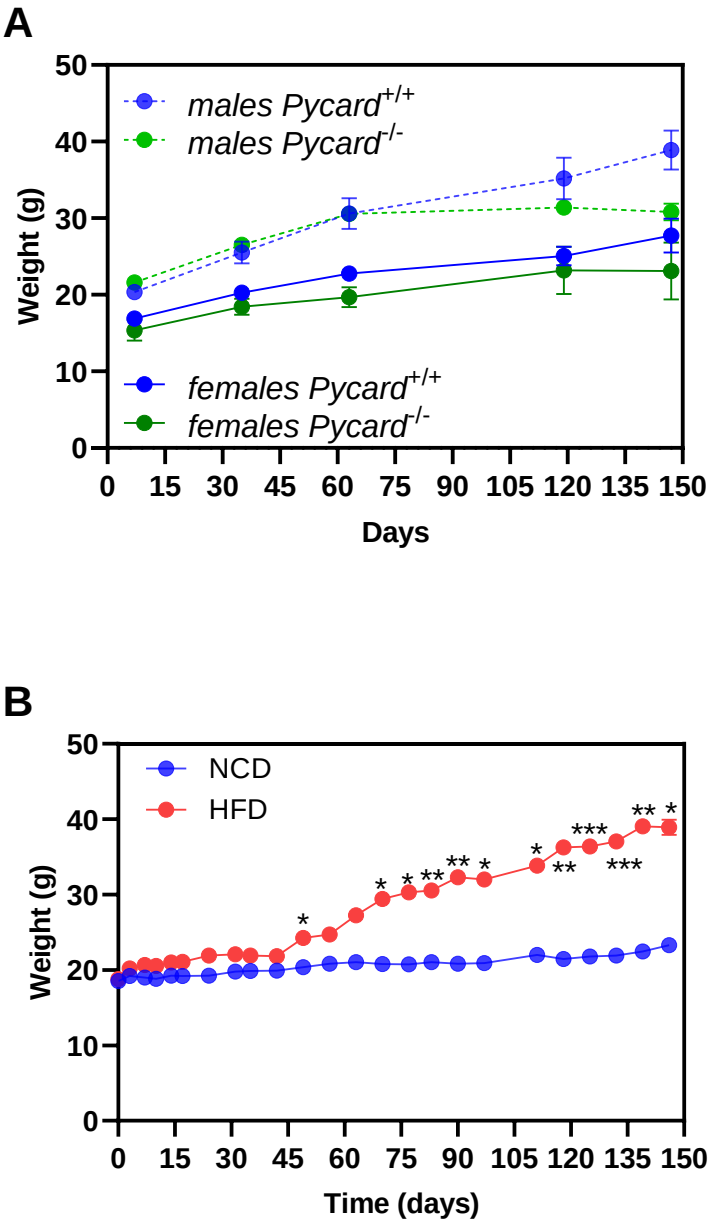

# Supplementary Figure 2

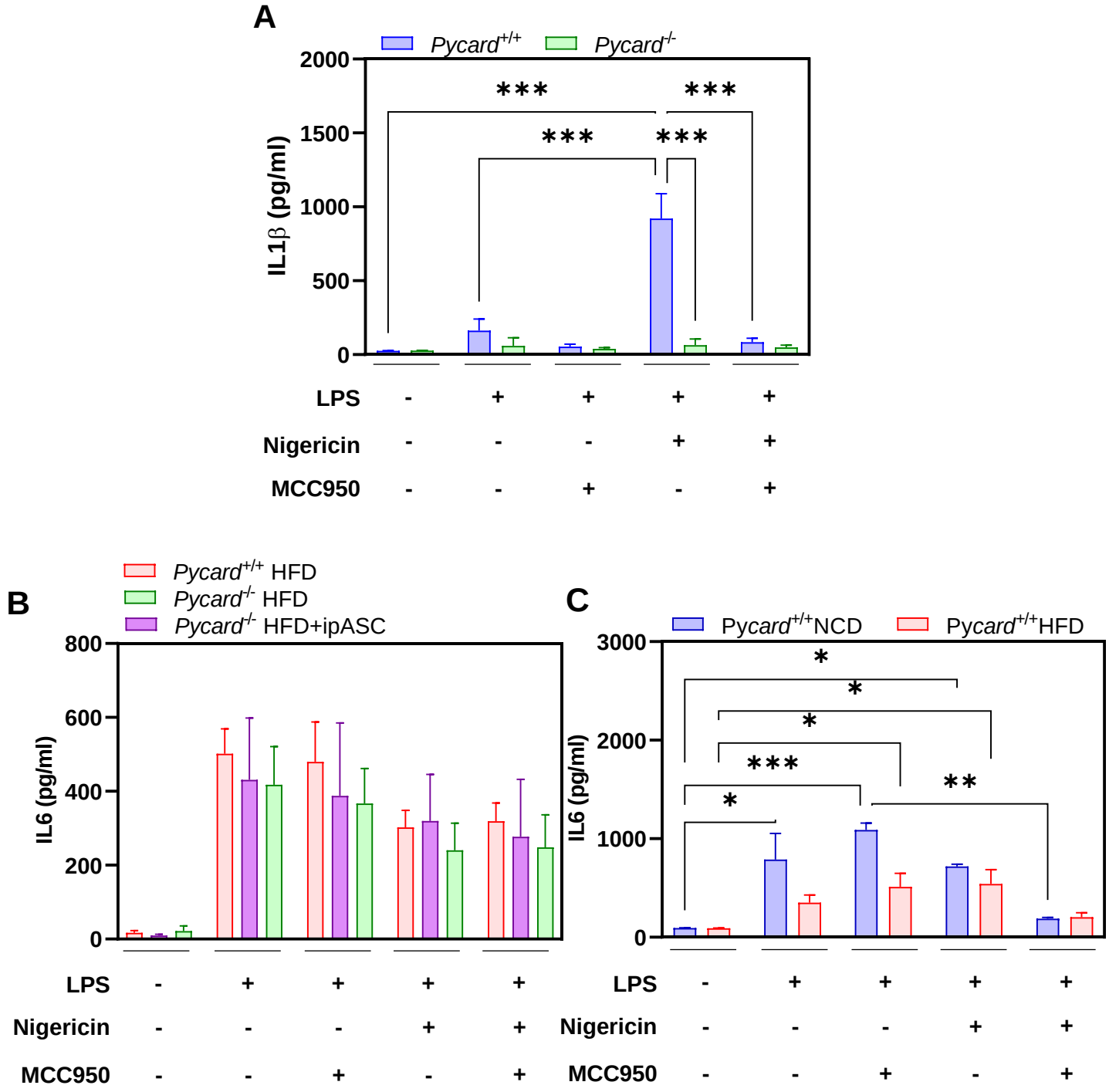

# Supplementary Figure 3

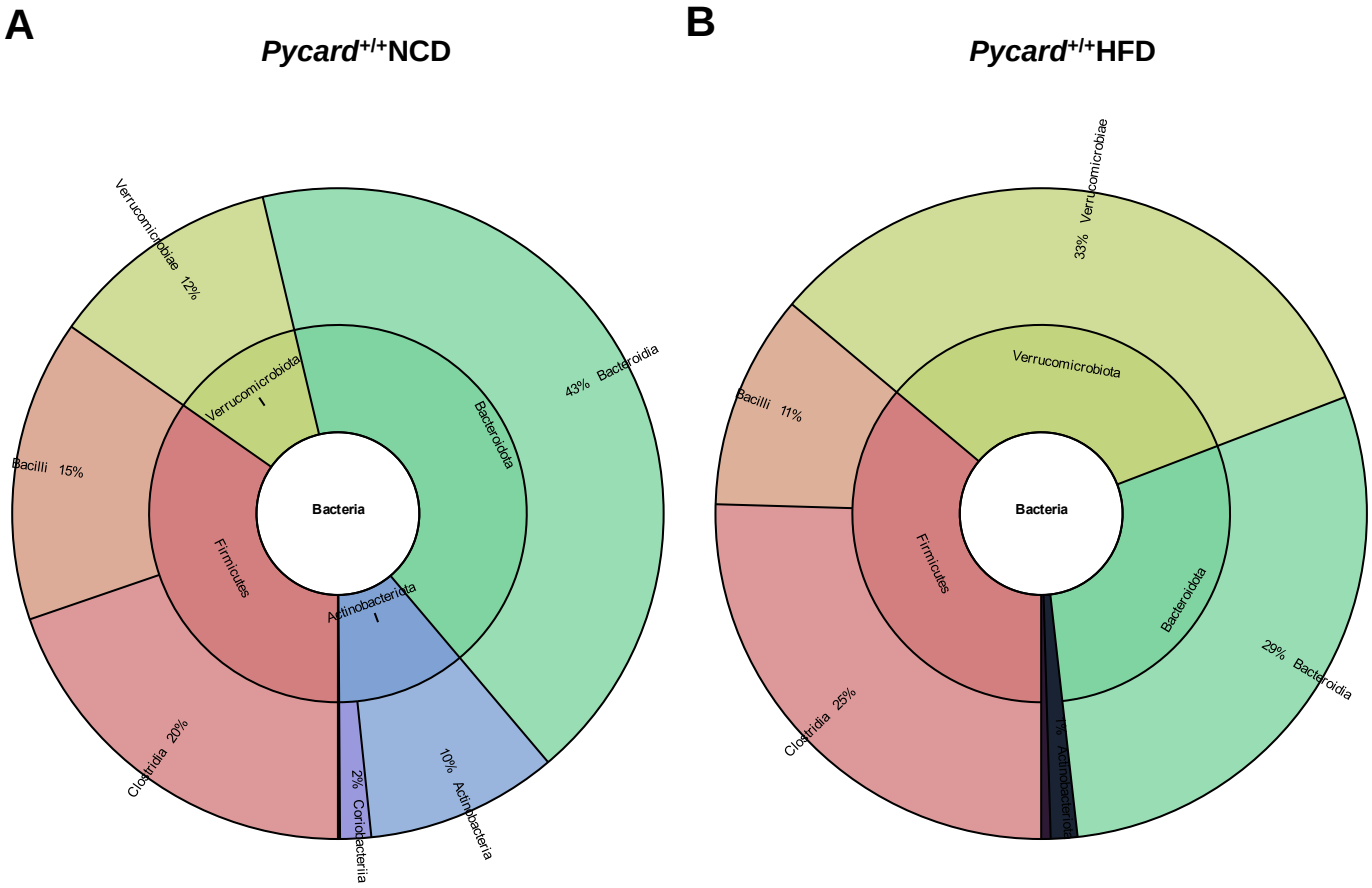


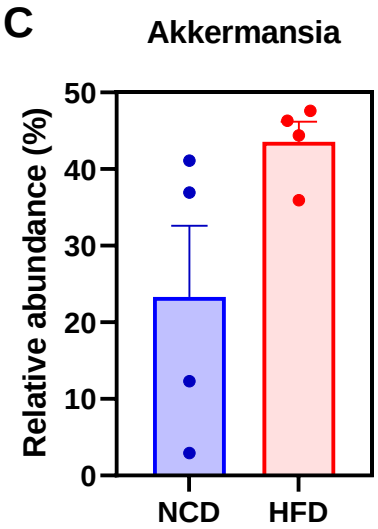

# Supplementary Figure 4

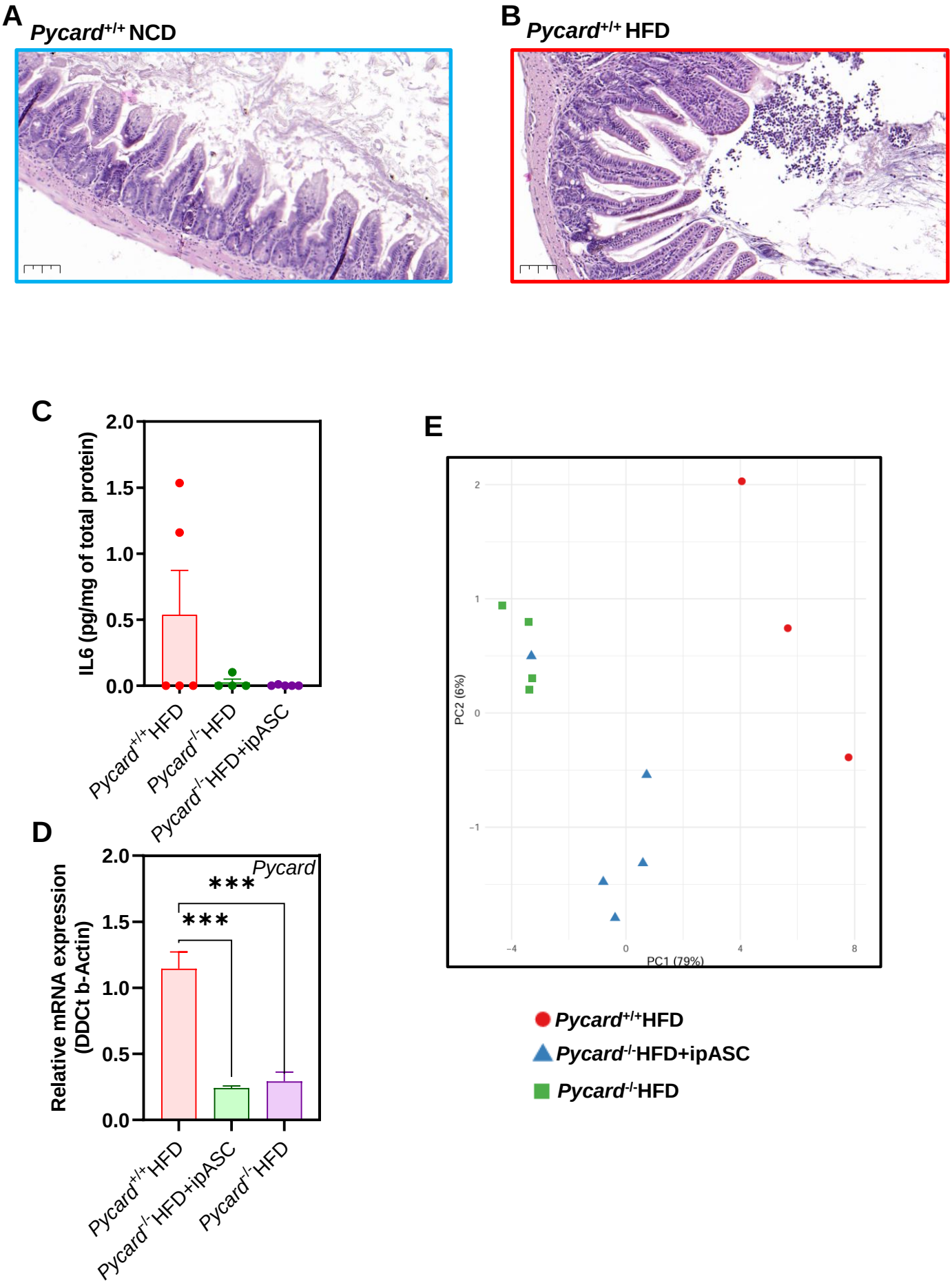

# Supplementary Figure 5

**A** ***Pycard*$^{+/+}$ NCD**

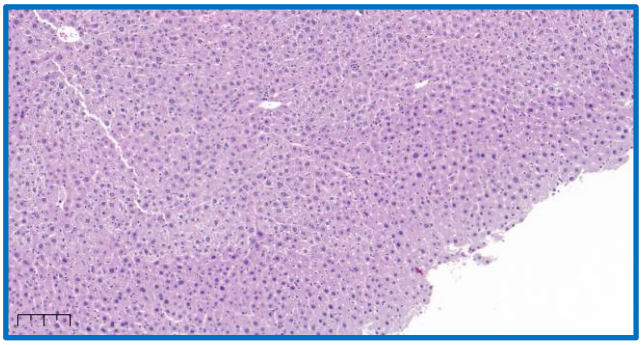
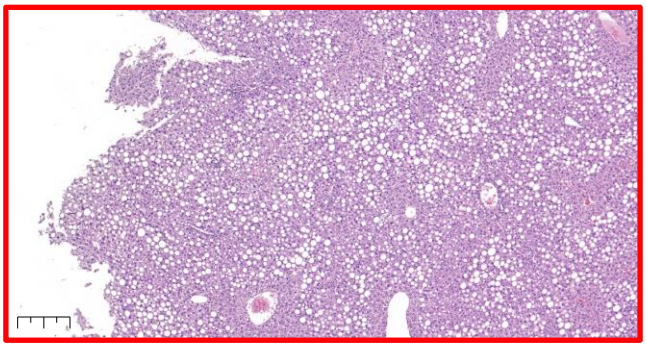
**B** ***Pycard*$^{+/+}$ HFD**